International Communications in Heat and Mass Transfer 169 (2025) 109764

Contents lists available at ScienceDirect

International Communications in Heat and Mass Transfer

journal homepage: www.elsevier.com/locate/ichmt

Design optimization and performance analysis of a PCM-to-air heat exchanger with optimized fin configuration for building heating applications

Mohamed Ahmed Said [a], Jasim M. Mahdi [b], Marrwa S. Ghanim [c], Khalil Hajlaoui [d,*], Nashmi H. Alrasheedi [d], Mohammad Ghalambaz [e,*], Pouyan Talebidadehsardari [f], Nidhal Ben Khedher [g]

[a] Architectural Engineering Department, University of Ha'il, Ha'il, Saudi Arabia
[b] Department of Energy Engineering, University of Baghdad, Baghdad 10071, Iraq
[c] Scientific Research Commission, Baghdad 10071, Iraq
[d] College of Engineering, Imam Mohammad Ibn Saud Islamic University (IMSIU), Riyadh, Saudi Arabia
[e] Department of Mathematical Sciences, Saveetha School of Engineering, SIMATS, Chennai, India
[f] Power Electronics, Machines and Control (PEMC) Institute, University of Nottingham, Nottingham, UK
[g] Department of Mechanical Engineering, University of Ha'il, Ha'il, Saudi Arabia

ARTICLE INFO

Keywords:
Phase change material
Building heating applications
Thermal energy storage
Fin configuration
Air heating

ABSTRACT

This study investigates the design optimization and performance enhancement of a novel triplex-tube phase change material (PCM)-to-air heat exchanger with optimized longitudinal fin configurations for building heating applications. Comprehensive numerical simulations were conducted to evaluate the influence of fin number, distribution, dimensions, and operating conditions on critical performance metrics. Seven fin configurations were analyzed under various Reynolds numbers (500–2000) and inlet air temperatures (0–10 °C). Results demonstrate that the optimal fin arrangement (10 fins inner pipe, 28 fins outer pipe) achieved 55.3 % reduction in PCM solidification time and 117.3 % increase in heat recovery rates compared to non-finned configurations. Increasing Reynolds number from 500 to 2000 enhanced overall heat recovery by 113 % while reducing solidification times by 45 %, though with a 14.3 % trade-off in peak outlet temperature. Decreasing inlet temperature from 5 °C to 0 °C improved total system heat recovery by 24.7 % and reduced solidification time by about 25 %. The study advances the field by introducing an innovative asymmetric PCM distribution across dual annular spaces with optimal fin arrangements, establishing critical design guidelines for high-performance PCM-based heating systems.

1. Introduction

The global building sector represents a critical focus for energy efficiency initiatives, accounting for approximately 32–33 % of total energy consumption worldwide, with space heating alone comprising 18–73 % of this demand depending on climate conditions and regional factors [1]. This substantial energy footprint translates directly to environmental impact, with building heating systems contributing around 40 % of global carbon dioxide emissions [2]. As international commitments to carbon neutrality intensify and energy costs continue to rise, developing efficient, sustainable building thermal management solutions has become increasingly urgent for both environmental sustainability and economic viability.

Among various emerging technologies addressing this challenge, thermal energy storage (TES) has gained significant attention as pivotal enabler of more sustainable building applications [3]. TES systems effectively decouple energy generation from utilization, allowing buildings to capture thermal energy during periods of excess availability and release it during peak demand, thereby optimizing energy distribution, and reducing peak loads [4]. Within the spectrum of TES

* Corresponding authors.
E-mail addresses: m.said@uoh.edu.sa (M.A. Said), jasim@siu.edu (J.M. Mahdi), marrwsalim@src.edu.iq (M.S. Ghanim), kmhajlaoui@imamu.edu.sa (K. Hajlaoui), nhrasheedi@imamu.edu.sa (N.H. Alrasheedi), m.ghalambaz@gmail.com (M. Ghalambaz), pouyan.talebizadehsardari2@nottingham.ac.uk (P. Talebidadehsardari), n.khedher@uoh.edu.sa (N. Ben Khedher).

https://doi.org/10.1016/j.icheatmasstransfer.2025.109764

Available online 16 October 2025

approaches, latent-heat TES (LHTES) utilizing phase-change materials (PCMs) offers particularly compelling advantages for building applications due to its exceptional thermal performance characteristics [5]. PCMs demonstrate remarkable energy density capabilities, storing 5–14 times more thermal energy per unit volume than conventional sensible TES materials while operating within narrow temperature fluctuations [6]. This near-isothermal operation during phase transitions aligns exceptionally well with human thermal comfort requirements and building heating demands [7]. These properties position PCM-based systems as highly promising solutions for addressing energy efficiency challenges in the building sector, particularly for space heating applications where they can capture excess thermal energy during off-peak periods and release it during peak demand, creating more stable and efficient thermal management.

Various PCMs have been explored for building heating applications [8,9]. Among these, organic PCMs, specifically paraffins have been most widely applied in building heating systems [10,11]. Paraffins offer favorable properties including suitable melting ranges (20–60 °C), negligible subcooling, chemical stability, non-corrosiveness, and long-term cycling reliability, making them particularly attractive for indoor thermal comfort applications [12]. However, these PCMs exhibit inherently low thermal conductivity (typically ranging from 0.2 to 0.4 W/m·K) [13,14], which substantially impairs heat transfer rates during both charging (melting) and discharging (solidification) processes. This limitation manifests as extended thermal response times that would fail to meet the dynamic heating demands of building environments, particularly during rapid temperature fluctuations or sudden heating requirements [15].

The heat transfer bottleneck in these materials is especially pronounced during solidification, where the growing solid PCM layer adjacent to heat transfer surfaces eliminates convective motion in the solidified region, making conduction is the dominating mechanism for heat removal in PCM systems [16]. This limitation significantly diminishes the practical utility of these systems in real-world building settings by extending discharge times beyond acceptable operational windows [17]. Furthermore, conventional PCM-based heat exchangers, such as shell-and-tube and double-tube designs, have been extensively investigated and provide useful baselines for performance evaluation. However, these traditional configurations often suffer from prolonged melting/solidification times and limited energy recovery efficiency when evaluated under uniform parameters such as heating power, melting rate, or thermal–hydraulic efficiency. These limitations restrict their applicability in dynamic building heating scenarios, where rapid thermal response and sustained energy delivery are essential.

To overcome these fundamental limitations, researchers have explored numerous heat transfer enhancement techniques for PCM systems, including the incorporation of high-conductivity additives such as metal particles or carbon-based materials [18], micro/macro encapsulation strategies to increase surface area-to-volume ratios [19], and various extended surface designs [20–22]. Among these approaches, finned heat exchangers have demonstrated considerable practical promise due to their manufacturing feasibility, relative cost-effectiveness, and substantial documented performance improvements [23]. The thermal performance of finned PCM heat exchangers depends on multiple interrelated parameters, including fin geometry, spacing, thickness, material properties, and spatial arrangement [24]. Developing an optimal configuration requires careful balancing of increased conductive pathways with sufficient PCM volume to maintain adequate energy storage capacity [25]. Furthermore, in air-based systems specifically, the fin arrangement must simultaneously enhance airside heat transfer while minimizing pressure drop to reduce fan power consumption and associated operational costs, adding another layer of design complexity [26,27].

Conventional PCM heat exchanger designs have predominantly employed shell-and-tube, plate, or compact configurations with single PCM compartments [28]. While these traditional arrangements have been extensively studied and incrementally improved, they still struggle to achieve the rapid thermal response necessary for building heating applications [29]. The triple-tube heat exchanger (TTHX) represents an emerging configuration that offers superior heat transfer area per unit volume and enables novel thermal energy transfer pathways that could potentially overcome the limitations of conventional designs [30]. Recent studies have explored conventional TTHXs for various applications and reported significant performance improvements compared to double-tube designs in terms of both energy transfer rates and thermal response times [31,32].

As summarized in Table 1, various fin configurations have been extensively studied to enhance PCM heat transfer in TTHXs, with researchers demonstrating significant performance improvements compared to non-finned designs. The configuration, orientation, dimensions, and material of fins play crucial roles in performance enhancement, with the most effective designs achieving 40–70 % reduction in melting/solidification times and 30–150 % increases in heat transfer rates compared to conventional systems. However, research on air-to-PCM heat transfer in triple-tube configurations remains remarkably scarce, with no comprehensive studies addressing the complex optimization requirements specific to building heating applications where air is the primary heat transfer medium [16].

This study introduces a novel triplex-tube TES system incorporating RT25HC as the PCM, specifically engineered for building heating applications to overcome the shortcomings of conventional structures and to provide a fair comparative framework for assessing performance improvements. Unlike previously studied configurations, the system

Table 1
Summary of fin configuration performance in TTHXs with PCMs.

Fin Configuration	Key Performance Enhancement	Geometric Parameters	Reference
Fractal H-shaped fins	69.14 % improvement in heat transfer performance	Optimized branching patterns	Triki et al. [33]
Staggered circular fins	59.1 % increase in heat storage rate; 37.2 % reduction in melting time	Longer fins (0.67 mm × 15 mm) vs base case (2 mm × 5 mm)	Xinguo et al. [34]
Branched fins	35 % reduction in melting time; 47.6 % increase in energy transfer rate	Optimum angles: α = 60°, β = 50°	Hussain et al. [35]
T-shaped fins	33.5 % reduction in melting time with 36 mm^2 less fin area	Optimum length: 30 mm; width: 45 mm; thickness: 0.5 mm	Fethi et al. [36]
Circular angled fins	44 % faster solidification time (1973 s)	17.5 mm length fins	Kaplan et al. [37]
Arc-shaped fins	17 % increase in melting rate vs rectangular fins; 93.1 % vs no fins	90° circular angle, inline distribution	Abed et al. [38]
Arch-shaped fins	53 % reduction in melting time; 117 % improvement in heat storage rate	Equal inner/outer fin base heights of 10 mm	Boujelbene et al. [39]
Annular fins	Optimal case (30 fins) achieved 85.8 % faster melting vs 4 fins	Additional fin at bottom improved performance	Abdullah et al. [40]
Leaf-vein inspired branched fins	23.8 % reduction in melting time; 28.8 % reduction in solidification time	Two branched fins with 140° angle	Hashim et al. [41]
Crossed snowflake fins	Increased PCM melting accumulation by 3.92 kJ; solidification exotherm by 5.77 kJ	Optimum length: 11 mm; width: 0.8 mm; bifurcation angle: 60°	Fang et al. [42]
Triangular fins	40 % acceleration of melting process	Eight triangular fins on inner and outer walls	Yan et al. [43]

innovatively distributes the PCM across two distinct annular spaces (inner and outer) with strategic asymmetric mass allocation (0.45 kg and 0.87 kg, respectively). This approach offers superior performance through three mechanisms: (1) thermal load distribution across multiple PCM compartments reduces individual compartment thermal stress and enables optimized fin arrangements, (2) asymmetric PCM mass allocation creates controlled thermal response sequencing for improved dynamic performance, and (3) dual annular heat transfer surfaces provide enhanced surface-to-volume ratios while maintaining compact system geometry. Longitudinal fins are implemented in these PCM domains to enhance thermal conductivity while maintaining a constant total fin volume across different configurations, enabling meaningful comparison among various enhancement techniques. The study also aims to investigate the influence of fin number, distribution, and dimensions on both steady-state and transient thermal performance of the proposed triplex-tube PCM-to-air heat exchanger. It examines how key design parameters and operating conditions (including Reynolds number and inlet air temperature) affect critical performance metrics, including heat recovery rate, PCM solidification time, outlet air temperature profile, and pumping power requirements. The findings provide valuable design guidelines for developing high-performance PCM-based heating systems that can effectively address the challenges of energy efficiency and thermal comfort in buildings while advancing the theoretical understanding of multi-compartment PCM heat exchanger design principles. Although traditional shell-and-tube and double-tube PCM heat exchangers have been widely studied, they often suffer from limited heat transfer surface area and prolonged thermal response times. The triplex-tube configuration proposed in this work aims to overcome these limitations by simultaneously extracting heat from dual PCM compartments, improving thermal gradients, and enabling tailored fin arrangements. This makes the design particularly relevant for building heating applications where both rapid response and sustained heat delivery are required.

2. Problem description

2.1. Triple-tube TES system configuration

This study investigates a novel triplex-tube TES system incorporating PCM (RT25HC) for heating applications. The heat exchanger is designed for boosting the air temperature used for heating in building's applications. Thus, the system consists of three concentric tubes creating a distinctive configuration with PCM contained in two annular spaces to heat the air from both inner and outer tubes. The inner pipe has an inner diameter of 50 mm with a 2 mm wall thickness, while the middle pipe features an inner diameter of 90 mm and a 2 mm wall thickness. The outer pipe has an inner diameter of 116.34 mm with a 2 mm wall thickness. As illustrated in Fig. 1(a) showing the case without fins in the PCM domain, the PCM fills both the inner and outer annular spaces, while air flows through the central channel. The outer pipe diameter was specifically selected to optimize the heat transfer area ratio between the middle tube and PCM tubes, ensuring balanced thermal performance. The PCM mass distribution between the two annular spaces is uneven: 0.45 kg in the inner pipe annular space and 0.87 kg in the outer pipe annular space. This asymmetric distribution significantly influences the thermal behavior of the system and guides the fin arrangement design needed to achieve uniform heat transfer. The entire design aims to efficiently recover and transfer thermal energy from the solidifying PCM to the incoming cold air stream.

To improve heat transfer between the PCM and airflow and also inside the PCM domain, longitudinal fins are incorporated in both PCM domains, as shown in Fig. 1(b). While the total fin volume remains constant across different configurations, the number and dimensions vary to optimize performance. For the baseline configuration (Case 1), the system includes 4 fins in the inner pipe with dimensions of 2.181 mm × 18.340 mm and 8 fins in the outer pipe with dimensions of 2.181 mm × 9.17 mm. The outer pipe contains more fins due to its larger PCM mass, providing enhanced heat transfer rates necessary for the outer annular space to achieve solidification times comparable to the inner annular space. As the number of fins increases across configurations, their thickness decreases proportionally to maintain constant volume, creating a design trade-off between heat transfer area and fin conduction effectiveness.

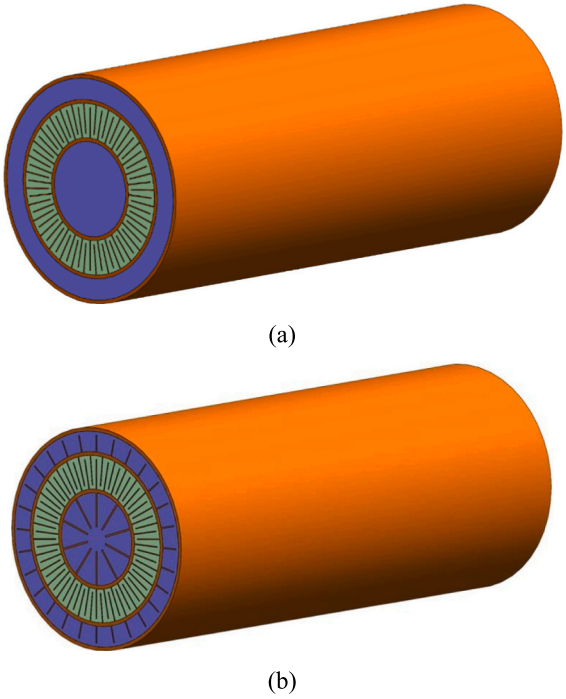

Fig. 1. Schematic of the triple-tube PCM system showing the tube arrangement and PCM distribution: (a) without fins, and (b) with longitudinal fins.

This triple-tube design is expected to improve performance through three fundamental mechanisms: (1) The simultaneous heat extraction from both annular spaces creates enhanced thermal gradients that cannot be achieved in conventional single-compartment designs, (2) The central air channel receives thermal energy from both PCM domains, creating a more uniform temperature distribution compared to conventional designs, and (3) The asymmetric PCM distribution enables controlled solidification sequencing where the inner pipe provides rapid initial response while the outer pipe sustains longer-duration energy release. RT25HC was selected as the PCM based on both thermal performance and operational compatibility with building heating systems. It has a phase-change temperature range (22–26 °C solidus-liquidus), which aligns closely with typical indoor comfort temperatures (20–24 °C) as specified by ASHRAE 55 standards [44]. Furthermore, it has a relatively high latent heat of fusion (230 kJ/kg) [45], which offers good energy storage density for space heating applications. Table 2 lists the key thermophysical properties of RT25HC.

The storage unit optimized in this study represents a simplified,

Table 2
Thermophysical properties of the PCM (RT25HC) used in the triple-tube TES setup [45].

Property	Value
ρ (kg/m^3)	880 (solid) / 770 (liquid)
k (W/m.K)	0.2
C_p (J/kg K)	2000
β_T (K^{-1})	0.0005
μ [N.s/m^2]	0.035
L_f (J/kg)	230,000
T_m (°C)	22 (solidus) / 26 (liquidus)

scaled-down model of a more complex system that integrates multiple triple-tube TES units. The proposed triplex-tube configuration is compatible with conventional fabrication techniques. The three concentric tubes can be manufactured by roll-forming, and the longitudinal fins can be fabricated via extrusion and then attached by standard welding or brazing. In the full-scale application, these units can be arranged in parallel and series configurations, depending on the size and thermal requirements of the building. Fig. 2 illustrates a schematic of the operational configuration of the system designed for applications in building in combination with other components required for the storage unit and also integrated with a solar system. The system comprises a heating solar collector with circulation fan, the TES unit with circulation fan, the fresh air supply and the building. In this setup, the PVT module serves to produce both electricity and heat required in the building. Electricity is required to circulate air across the system. The heat is transferred to the storage system to be then used during the high-demand hours. The TES is used to discharge heat to the air used for heating in the building. During the charge mode, the heat generated in the solar collector is transferred to the TES. By integrating the TES unit with the PVT module, it becomes capable of supplying the heat required for the heating load and hot air demand. This study is focused on the discharging performance of PCM for heating purpose to prove the capability of this system in providing the heating demand of the building using air as the heating fluid.

2.2. Simulation cases

2.2.1. Steady-state analysis cases

The steady state analysis focuses on evaluating the air flow and heat transfer characteristics with constant wall temperature conditions of 25 °C. The aim of steady-state simulation is to reach the optimum case for the air flow in the middle pipe to prevent unnecessary computational cost of simulating the entire domain. For this purpose, seven configurations (SS0-SS7) are evaluated to determine the optimal number of fins and pipe length, as illustrated in Figs. 3 and 4. Configurations SS0 through SS3 examine the effect of increasing the number of fins from 16 to 32 while maintaining a constant pipe length of 300 mm. This allows for assessment of how fin density affects outlet temperature and pressure drop. Configurations SS3 through SS5 investigate the effect of fin length variation from 16 mm to 8 mm while maintaining 32 fins. This series of tests helps identify the optimal fin dimensions to balance heat transfer and flow resistance. Furthermore, configurations SS3, SS6, and SS7 focus on the effect of pipe length variation from 300 mm to 200 mm and 400 mm with 32 fins. These tests provide insight into how the heat exchanger length influences the outlet temperature and overall thermal performance.

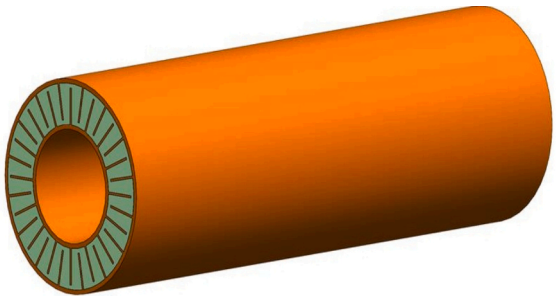

Fig. 3. Schematic of the steady-state analysis setup showing the air-flow configuration.

2.2.2. Transient analysis cases

Seven configurations (Cases 0–6) are numerically examined to evaluate the dynamic performance during PCM solidification as heat transfers from the initially liquid PCM at 25 °C to the colder airflow, as shown in Fig. 5 and Table 3. Cases 0 through 4 implement a progressive increase in fins' numbers, starting from no fins in Case 0 to 10 fins in the inner pipe and 20 fins in the outer pipe for Case 4. This progression reveals how fin density influences the solidification rate and heat recovery. Cases 4 through 6 maintain fixed inner pipe fins at 10 while increasing outer pipe fins from 20 to 28. This series focuses on optimizing the outer pipe performance since it contains nearly twice the PCM mass of the inner pipe. Additional parametric studies explore the effect of Reynolds number variation ($Re = 500, 1000, 2000$) and air inlet temperature variation (0 °C, 5 °C, 10 °C). These studies provide valuable insight into how operational conditions affect the system performance.

2.3. Performance metrics

The system's performance is evaluated using several key metrics. The

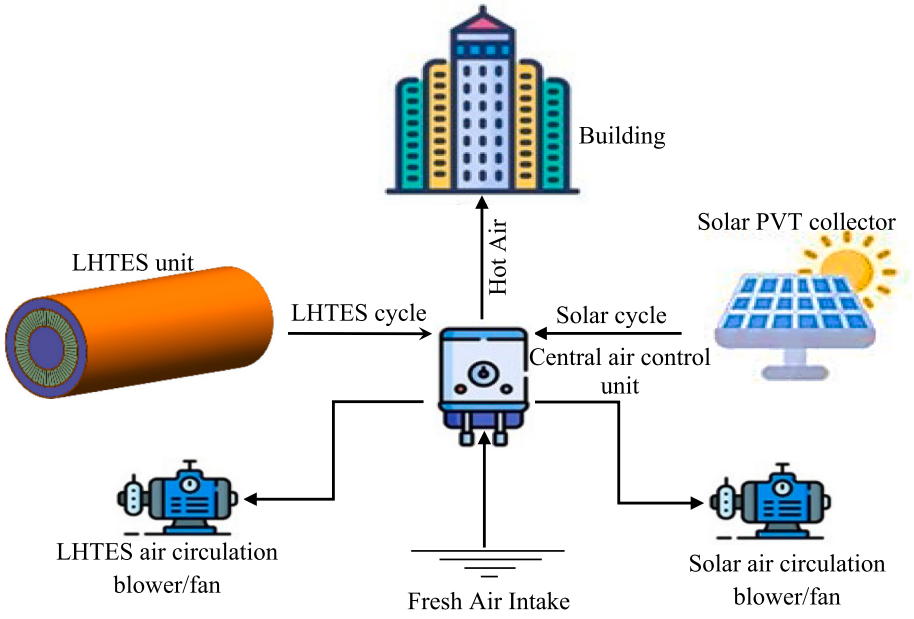

Fig. 2. A schematic of system operation for building heating applications.

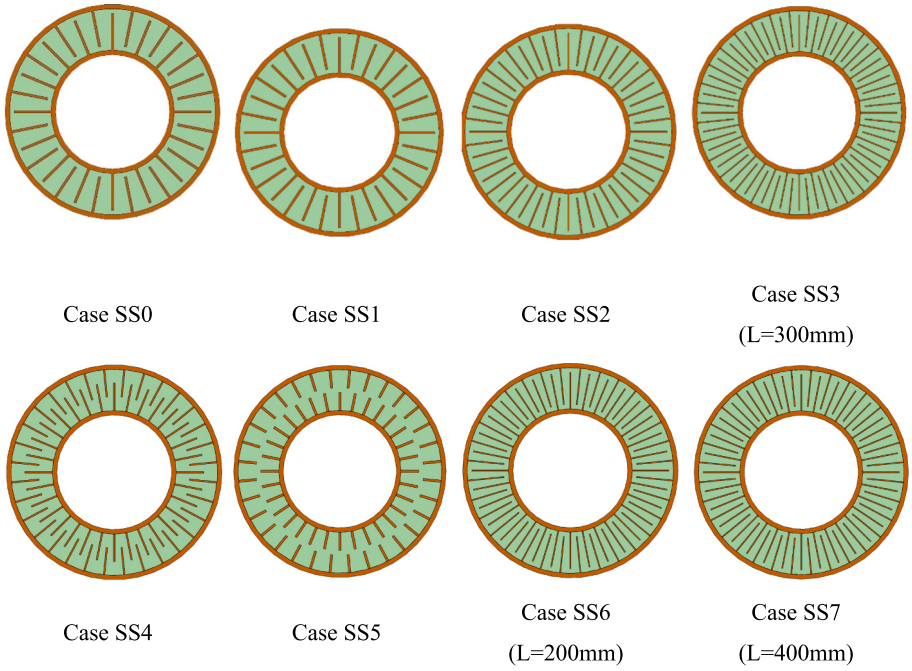

Fig. 4. Cross-sectional views of eight fin configurations (SS0-SS7) for steady-state analysis showing varying fin numbers, fin dimensions, and pipe lengths.

air outlet temperature profile over time directly relates to the usefulness of the heat exchanger for heating applications. PCM solidification time serves as a critical metric for system recharging requirements. Heat recovery rate quantifies the thermal energy extracted from the PCM during operation. Liquid fraction evolution provides insights into how the phase change process progresses within the different regions of the heat exchanger. The objective is to identify a configuration that maximizes heat recovery while achieving complete PCM solidification within the operational timeframe of 2–3 h. This balances thermal performance with PCM storage efficiency to create a practical triple-tube PCM heat exchanger design.

3. Mathematical model and boundary conditions

3.1. Phase-change governing equations

The phase change process of PCM within the TTHX system is modeled using the governing conservation equations with enthalpy-porosity technique by Brent et al. [46] to capture the behavior of PCM solidification. This approach models the mushy zone (the partially solidified region) as a porous medium, where the porosity is defined by the local liquid fraction, effectively modeling the gradual transition between solid and liquid states without explicitly tracking the moving solid-liquid interface. For both the PCM domains and airflow channel, the conservation of mass is expressed as:

$$\frac{\partial \rho}{\partial t} + \nabla \cdot \left(\rho \vec{V} \right) = 0 \tag{1}$$

where ρ represents the density, t is time, and $\vec{V}$ denotes the velocity vector.

The momentum conservation equation for the PCM domain incorporates the Boussinesq approximation for natural convection effects and includes a momentum sink term to account for the phase change process:

$$\rho \frac{\partial \vec{V}}{\partial t} + \rho \left(\vec{V} \cdot \nabla \right) \vec{V} = -\nabla P + \mu \left(\nabla^2 \vec{V} \right) + \rho \beta (T - T_{ref}) \vec{g} - \vec{S} \tag{2}$$

where P represents pressure, μ is dynamic viscosity, β is the thermal expansion coefficient, T is temperature, T_{ref} is the reference temperature for the Boussinesq approximation, $\vec{g}$ is the gravitational acceleration vector, and $\vec{S}$ is the momentum sink term formulated according to the Carman-Kozeny equation for flow through porous media. The Boussinesq approximation is valid since maximum density variation ($\beta \Delta T = 5 \times 10^{-4} \times 26\ ^{\circ}C$) $< < 5\ \%$ criterion for natural convection applications in in PCM systems [46].

The momentum sink term $\vec{S}$ is defined as:

$$\vec{S} = A_m \frac{(1-\lambda)^2}{\lambda^3 + \epsilon} \vec{V} \tag{3}$$

where A_m is the mushy zone constant (set to 10^5 kg/m^3·s), λ is the liquid fraction, and ϵ (typically 0.001) is a small computational constant to prevent division by zero when the liquid fraction approaches zero. This formulation effectively damps velocity in partially solidified regions and reduces it to zero in fully solidified regions. The value of A_m was set to 10^5 kg/m^3·s based on the literature-recommended range (10^4–10^7) [47]. This value also provided good agreement with the experimental results of Longeon et al. [48] and *Al*-Abidi et al. [49] used for validation, as demonstrated in Section 3.3.

The energy conservation equation accounts for both sensible and latent heat effects during the phase change process:

$$\rho C_p \frac{\partial T}{\partial t} + \nabla \cdot \left(\rho C_p \vec{V} T \right) = \nabla \cdot (k \nabla T) - S_L \tag{4}$$

where C_p is the specific heat capacity, k is the thermal conductivity, and S_L represents the latent heat source term associated with phase change.

The latent heat source term S_L is formulated as:

$$S_L = \rho \frac{\partial (\lambda L_f)}{\partial t} + \rho \nabla \cdot \left(\vec{V} \lambda L_f \right) \tag{5}$$

where L_f is the latent heat of fusion of the PCM.

The liquid fraction λ is calculated based on the temperature field using a piecewise linear function to model the mushy zone between solidus and liquidus temperatures:

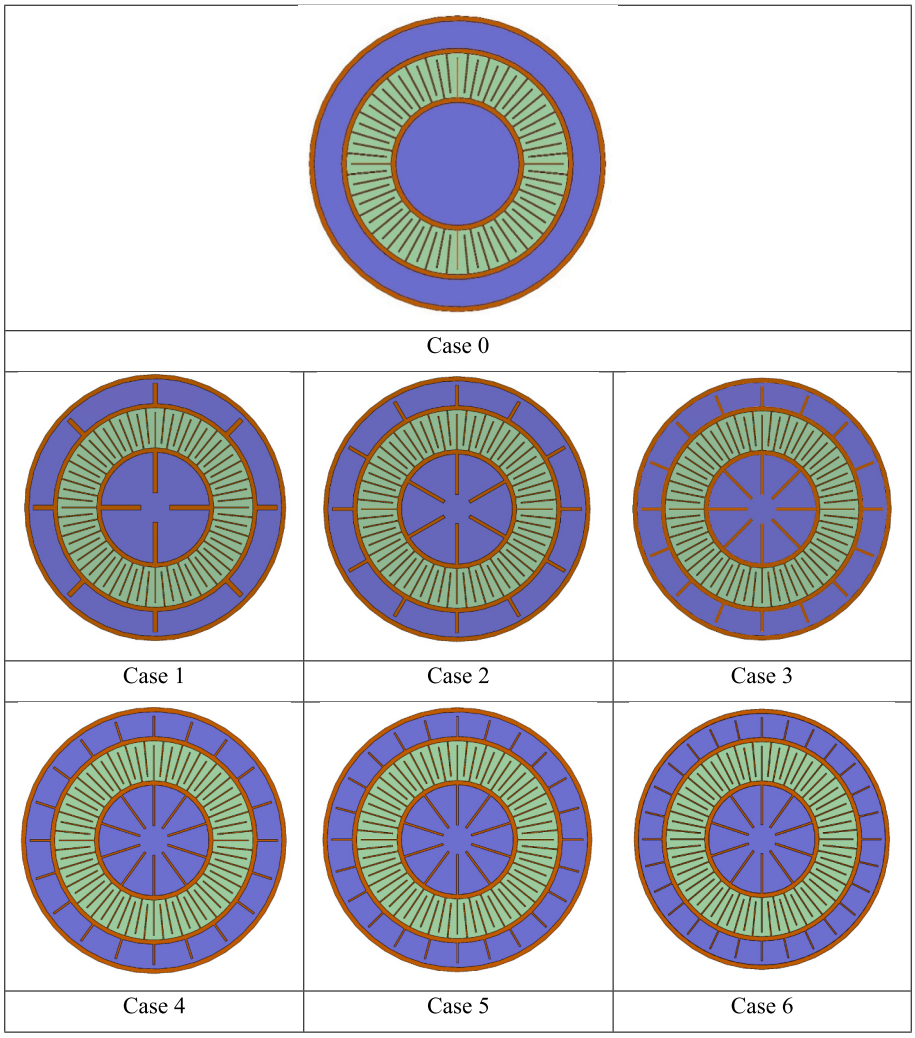

Fig. 5. Cross-sectional views of seven triple-tube configurations (cases 0–6) with varying fin numbers and arrangements.

Table 3
Study cases for transient simulations: distribution of fins in inner and outer pipes.

	Case 0	Case 1	Case 2	Case 3	Case 4	Case 5	Case 6
Number of fins in inner pipe	0	4	6	8	10	10	10
Number of fins in outer pipe	0	8	12	16	20	24	28

$$\lambda = \frac{\Delta H}{L_f} = \begin{cases} 0 \; if \; T < T_{Solidus} \\ 1 \; if \; T > T_{Liquidus} \\ \dfrac{T - T_{Solidus}}{T_{Liquidus} - T_{Solidus}} \; if \; T_{Solidus} < T < T_{Liquidus} \end{cases} \tag{6}$$

where ΔH represents the change in enthalpy, T_{Solidus} is the solidus temperature (22 °C for RT25HC), and T_{Liquidus} is the liquidus temperature (26 °C for RT25HC).

The total enthalpy of the PCM is computed as the sum of sensible enthalpy (h_{sensible}) and latent heat content (ΔH):

$$H = h_{\text{sensible}} + \Delta H = h_{\text{ref}} + \int_{T_{\text{ref}}}^{T} C_p dT + \lambda L_f \tag{7}$$

where h_{ref} is the reference enthalpy at the reference temperature.

For natural convection in the liquid PCM, the Boussinesq approximation is employed to model density variations that drive buoyancy-induced flows:

$$\rho = \rho_{\text{ref}}\left[1 - \beta\left(T - T_{\text{ref}}\right)\right] \tag{8}$$

where ρ_{ref} is the reference density at temperature T_{ref}. This approximation is valid for small temperature differences where density variations are only significant in the buoyancy term of the momentum equation.

3.2. Heat transfer fluid (air) governing equations

For the air flowing through the central channel, the governing equations follow the standard form of the Navier-Stokes equations, without the phase change terms:

$$\frac{\partial \rho}{\partial t} + \nabla \cdot \left(\rho \vec{V}\right) = 0 \tag{9}$$

$$\rho \frac{\partial \vec{V}}{\partial t} + \rho\left(\vec{V} \cdot \nabla\right)\vec{V} = -\nabla P + \mu\left(\nabla^2 \vec{V}\right) \tag{10}$$

$$\rho C_p \frac{\partial T}{\partial t} + \nabla \cdot \left(\rho C_p \vec{V} T\right) = \nabla \cdot (k \nabla T) \tag{11}$$

Air properties are treated as temperature-dependent to account for

variations across the temperature range encountered in the system. Laminar flow is assumed since maximum Reynolds number (2000) is below critical transition value (Re_{crit} = 2300–3000) for annular geometries.

3.3. Performance metrics

3.3.1. Heat recovery rate

The rate of thermal energy storage or release during the phase change process is quantified as:

$$\dot{E}_T = \frac{E_e - E_i}{t_m} \tag{12}$$

where t_m is the phase change duration, and E_e and E_i are the total thermal energy content of the PCM at the end and beginning of the phase change process, respectively. The total thermal energy includes both sensible and latent components:

$$E = \int_{V_{PCM}} \rho\left[C_p\left(T - T_{ref}\right) + \lambda L_f\right] dV \tag{13}$$

where V_{PCM} is the PCM volume.

3.3.2. Energy efficiency ratio (EER)

The energy efficiency ratio (EER) is defined as the ratio of useful thermal energy recovered to electrical energy consumed for pumping as:

$$EER = \frac{\dot{Q}recovered}{\dot{W}pumping} = \frac{\dot{E}inner + \dot{E}outer}{\Delta P \cdot \dot{V}} \tag{14}$$

where $\dot{Q}recovered$ *is the total heat recovery rate,* $\dot{W}pumping$ is the pumping power, ΔP is pressure drop, and $\dot{V}$ is volumetric flow rate.

3.3.3. Solidification time

The solidification time is defined as the time required for the average liquid fraction of the PCM to reach a specified threshold value (typically 0.05), indicating near-complete solidification:

$t_{solidification} = t$ at which $\bar{\lambda} \leq \lambda_{threshold}$

where $\bar{\lambda}$ is the volume-averaged liquid fraction.

3.4. Boundary and initial conditions

At the beginning of the simulation (t = 0), the following initial conditions are applied:

a. The PCM is in a fully liquid state (λ = 1) at a uniform temperature of 25 °C
b. The HTF (air) is at the specified inlet temperature (varied between 0 °C and 10 °C)
c. Zero velocity is prescribed for both the PCM and air domains

The following boundary conditions are imposed on the computational domain:

1. Air Inlet: Uniform velocity corresponding to the specified Reynolds number (Re = 500, 1000, or 2000) with constant inlet temperature (varied as 0 °C, 5 °C, or 10 °C).
2. Air Outlet: Zero gauge pressure condition
3. Solid Walls: No-slip condition ($\vec{V} = 0$ at all solid walls) with adiabatic condition at the outer boundary of the system (assuming perfect insulation)
4. Interfaces: Continuity of temperature and heat flux at material interfaces:

$$T_i = T_{i+1} \text{ and } k_i \frac{\partial T_i}{\partial n} = k_{i+1} \frac{\partial T_{i+1}}{\partial n}$$

where indices i and i + 1 represent adjacent materials, and n is the normal direction to the interface.

4. Numerical methodology

4.1. Numerical solution framework

The governing equations regulating the thermal exchange system and phase change development were solved using the commercial CFD solver ANSYS-FLUENT V. 2023R1. The coupled heat transfer and fluid flow phenomena were modeled using a finite volume method with a pressure-based solver approach. For the PCM domains, the enthalpy-porosity technique was implemented to track the progress of the solid-liquid interface without explicitly defining the moving boundary conditions. The SIMPLE algorithm was employed to handle pressure-velocity coupling, which is particularly suitable for pseudo-transient simulations of the type conducted in this study. For spatial discretization, the QUICK scheme was utilized for the momentum and energy equations due to its high-order accuracy. The pressure field was discretized using the PRESTO scheme, which is well-suited for flows involving steep pressure gradients commonly encountered in natural convection within melting PCMs.

For temporal discretization in the transient simulations, a first-order implicit scheme was used, providing unconditional stability regardless of the time step size. The convergence criteria were carefully established to ensure the accuracy of the numerical solution. Scaled residuals of 10^{-4} were set as the convergence threshold for both the continuity and momentum equations, while a more stringent criterion of 10^{-6} was applied to the energy equation due to its critical role in capturing the phase change phenomena and heat transfer processes. Under-relaxation factors of 0.3, 0.7, and 1.0 were applied to pressure, momentum, and energy equations, respectively, to enhance numerical stability while maintaining reasonable convergence rates.

4.2. Mesh independence analysis

The computational domain was discretized using uniform hexahedral elements in regular regions and near the fins. A mesh independence test was conducted separately for the steady-state and transient simulations to ensure that the numerical solutions were independent of the spatial discretization. For the steady-state analysis of the air section, four mesh densities with approximately 350,000, 440,000, 610,000, and 750,000 cells were evaluated using Case SS1 (Fig. 6) at a Reynolds number of 2000, which represents the most challenging flow condition in terms of numerical stability and accuracy. The key performance metrics monitored were the outlet air temperature and pressure drop across the heat exchanger, as these parameters directly affect the thermal-hydraulic performance of the system. As presented in Table 4, there was a notable difference in outlet temperature between the 350,000 and 440,000 cell meshes (22.38 °C versus 22.48 °C, representing a 0.45 % increase). Similarly, the pressure drop increased from 1.96 Pa to 1.97 Pa (0.51 % increase). However, further refinement to 610,000 and 750,000 cells resulted in negligible changes in both outlet temperature (less than 0.05 % variation) and pressure drop (less than 2.5 % variation). Based on these results, the 440,000-cell mesh was determined to provide an optimal balance between computational efficiency and solution accuracy for the steady-state simulations.

For the more computationally intensive transient simulations involving phase change phenomena, three mesh densities with approximately 880,000, 1,000,000, and 1,220,000 cells were evaluated using a

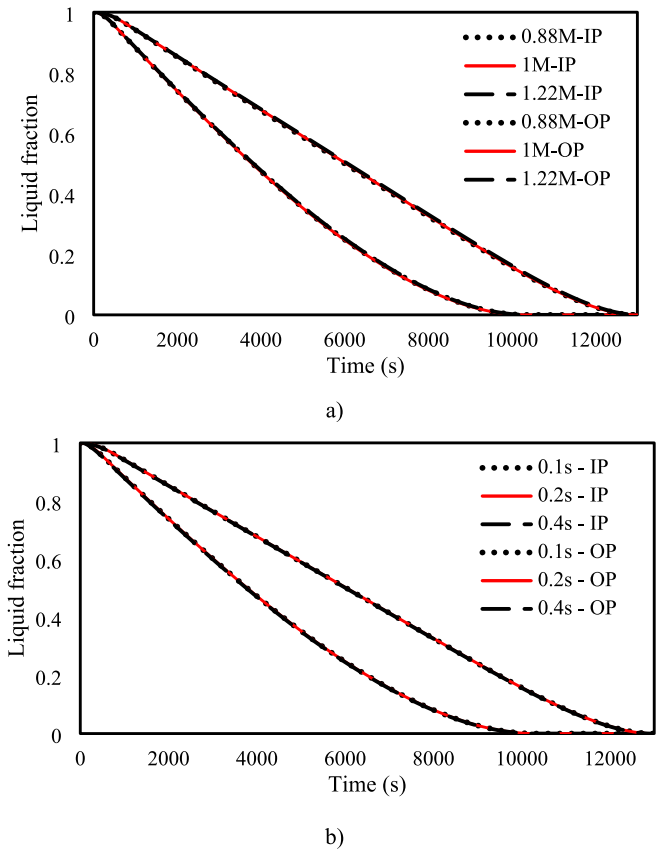

Fig. 6. Effect of a) number of cells and b) time step sizes on the liquid fraction of PCM in the inner and outer pipes.

Table 4
Mesh independence study for the air section using steady state simulation.

Number of cells	Outlet Temp. (°C)	Pressure drop (Pa)
350,000	22.38	1.96
440,000	22.48	1.97
610,000	22.47	2.01
750,000	22.48	2.02

constant time step size of 0.2 s. The liquid fraction evolution in both the inner pipe (IP) and outer pipe (OP) PCM domains was monitored as the primary indicator of mesh independence, as this parameter directly characterizes the phase change dynamics and overall system performance. As illustrated in Fig. 6a, the liquid fraction profiles for all three mesh densities showed excellent agreement throughout the entire simulation period (0–10,000 s) for both the inner and outer pipe PCM domains. The maximum deviation in liquid fraction between 880,000 and 1,000,000 cell meshes was less than 2 %, while the difference between the 1,000,000 and 1,220,000 cell meshes was less than 0.8 %. Considering these minimal variations and the substantial increase in computational resources required for the finer mesh, the 1,000,000-cell mesh was selected as the optimal discretization for the transient simulations, providing a good compromise between solution accuracy and computational efficiency.

Following the establishment of spatial discretization independence, a time step sensitivity analysis was performed to determine the optimal temporal resolution for the transient simulations. Using the selected 1,000,000-cell mesh, three different time-step sizes (0.1, 0.2, and 0.4 s) were evaluated by monitoring the liquid fraction evolution in both PCM domains. As shown in Fig. 6b, the liquid fraction profiles for all three different time-step sizes demonstrated excellent agreement throughout the simulation period for both the inner and outer pipe PCM domains. The maximum discrepancy between the 0.1-s and 0.2-s time steps was less than 1.5 %, while the difference between the 0.2-s and 0.4-s time steps was approximately 2.1 %. Given these minimal variations and considering the computational efficiency, the 0.2-s time step was selected as the optimal temporal resolution for all subsequent transient simulations.

4.3. Model validation

To validate the numerical methodology employed in this study, a comprehensive comparison was first conducted against the experimental findings of Longeon et al. [48] on melting of RT35 PCM in a double-tube heat exchanger system. Their experimental setup involved water flowing through the internal tube and PCM contained in the annular space between the two tubes. Fig. 7(a) shows a comparison of the PCM temperature evolution during the melting mode as predicted by the current numerical model against the experimental measurements. The results demonstrate excellent agreement throughout the entire melting duration, with a maximum deviation of approximately 2 % occurring during the intermediate stages of melting (between 3000 and 5000 s). The close correspondence between the numerical predictions and experimental data confirms the accuracy of the enthalpy-porosity approach and the associated numerical procedures implemented in this study.

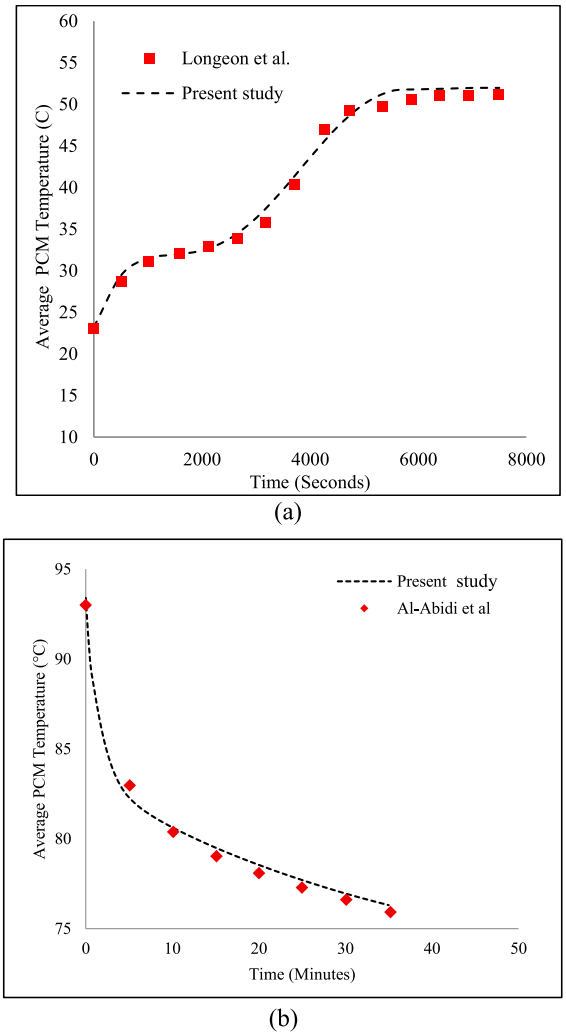

Fig. 7. Validation of the numerical model parameters against experimental data from (a) from Longeon et al. [48] and (b) *Al*-Abidi et al. [49].

Additional validation was conducted using selected data from *Al-Abidi et al.* [49] experiments on solidification of RT82 in a triplex tube heat exchanger with longitudinal fins. Their experimental setup featured water as the heat transfer fluid flowing at 68 °C through both inner and outer annular spaces, with RT82 PCM contained in the middle annulus enhanced by four longitudinal fins on each side. Fig. 7(b) illustrates the comparison between numerical predictions and experimental temperature measurements within the PCM domain during the solidification phase. The maximum deviation was determined as 1.8 %, well within acceptable limits for PCM thermal modeling applications. This validated numerical methodology forms a reliable foundation for the subsequent parametric studies investigating the effects of fin configuration, Reynolds number, and inlet temperature on the thermal performance of the proposed TTHE system.

5. Results and discussion

5.1. Steady-state simulation of the air passage

This section focuses on steady state analysis of the air flow characteristics within the TTHX configuration. This approach isolates the air-side heat transfer mechanisms, allowing for systematic evaluation of critical design parameters including fin number, fin dimensions, and pipe length without the computational complexity of phase change dynamics. This analysis seeks to determine the configuration that achieves maximum outlet air temperature with acceptable pressure drop penalties, thereby establishing the optimal geometric design that balances thermal performance with pumping power requirements.

5.1.1. Effect of the number of fins

Fig. 8 presents temperature contour plots for four different fin configurations in the air channel of the triple-tube heat exchanger. Cross-sectional temperature distributions are shown for cases ranging from no fins (Case-SS0) to 32 fins (Case-SS3). The corresponding performance data for these cases is provided in Table 5. In Case-SS0 (no fins), poor heat distribution is observed with an outlet temperature of only 12.57 °C. When 16 fins are introduced in Case-SS1, outlet temperature increases sharply to 22.49 °C (78.9 % improvement), though pressure drop rises by 453 % to 1.96 Pa. Case-SS2 with 24 fins further improves outlet temperature to 24.19 °C, but pressure drop increases to 3.34 Pa. Case-SS3 (32 fins) achieves near-perfect heat transfer with 24.97 °C outlet temperature, but at the highest pressure drop of 4.54 Pa. The data demonstrates diminishing thermal returns with increasing fin numbers: the first 16 fins provide a 9.92 °C gain, while the additional 16 fins yield only 2.49 °C more. Temperature contours show progressively more uniform distribution with higher fin counts, but pressure drop increases disproportionately (1182 % increase from SS0 to SS3 versus 99.5 % temperature improvement), highlighting the critical thermal-hydraulic trade-off in heat exchanger design. This indicates that thermal requirements must be carefully balanced against pumping power constraints, especially in applications where energy efficiency is crucial.

The superior performance observed with increasing fin density, from Case-SS0 (0 fin) to Case-SS3 (32 fins), stems from fundamental heat transfer enhancement mechanisms. Longitudinal fins create conductive pathways that effectively extend the high-conductivity metal surfaces deep into the low-conductivity PCM domain (k_{PCM} = 0.2 W/m·K vs k_{fin} = 200 W/m·K). This geometric enhancement overcomes the primary limitation of organic PCMs by reducing the effective thermal resistance between the heat source and the bulk PCM. The temperature uniformity improvement observed in Cases SS1-SS3 results from the fins acting as thermal equalizers, redistributing thermal energy from high-temperature regions near the heat transfer surfaces to cooler interior regions. However, the diminishing returns beyond 24–32 fins occur because the fin effectiveness decreases as fins become thinner to maintain constant fin volume, while simultaneously increasing flow restriction that reduces convective heat transfer at the air-metal interface.

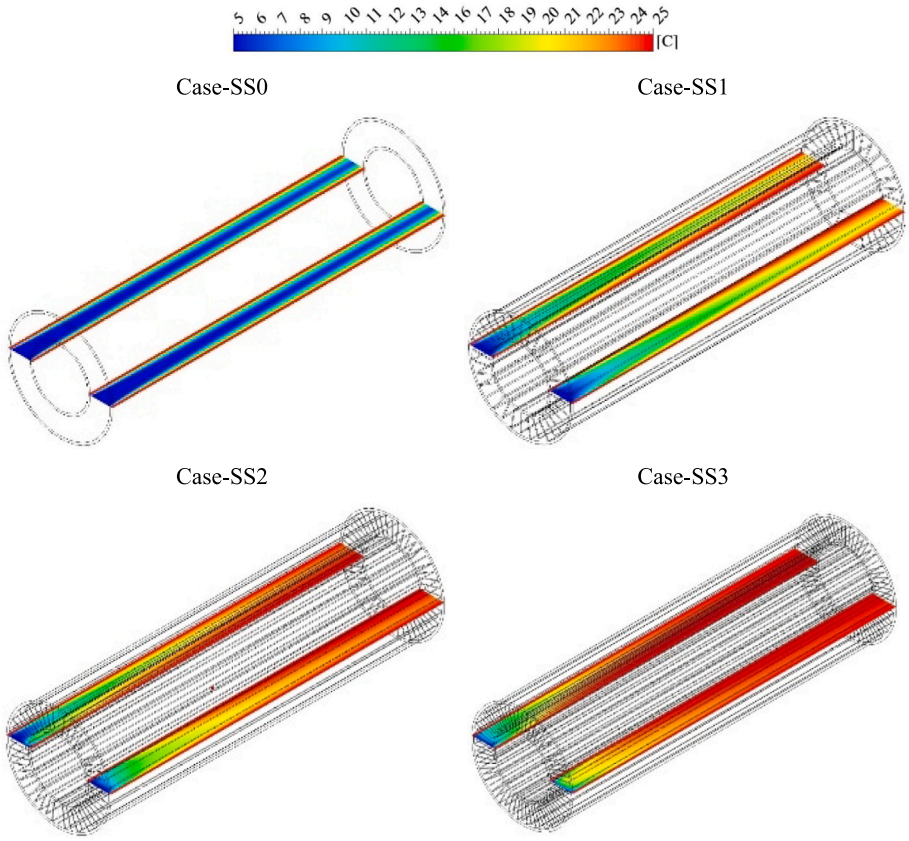

Fig. 8. Temperature distribution contours for varying fin configurations (Cases SS0-SS3) in the TTHX system.

Table 5
Effect of fin number on thermal-hydraulic performance parameters of the TTHX system.

Case	Fin's thickness (mm)	Fin's length (mm)	Number of fins	Pipe length (mm)	Outlet Temperature ($^{\circ}C$)	Mass flow rare (Kg/s)	Pressure drop (Pa)	Pumping power (W)
Case-SS0	–	–	0	300	12.5652	0.00379	0.35426	0.001098
Case-SS1	1	16	16	300	22.4867	0.003313	1.95917	0.005289
Case-SS2	0.6666	16	24	300	24.1927	0.003313	3.34034	0.009018
Case-SS3	0.5	16	32	300	24.9733	0.003313	4.54369	0.012267

5.1.2. *Effect of the fin's length*

The temperature contour plots of Fig. 9 reveal how fin length affects performance while maintaining 32 fins across three configurations (Case-SS3, Case-SS4 and Case-SS5). The performance data for these cases is provided in Table 6. In Case-SS3 (16 mm fins, 0.5 mm thickness), near-perfect heat transfer is achieved with an outlet temperature of 24.97 °C and pressure drop of 4.54 Pa. When fin length is reduced to 12 mm in Case-SS4 (with increased thickness of 0.6666 mm), outlet temperature decreases to 23.93 °C (4.2 % reduction), while pressure drop remains unchanged at 4.54 Pa. Further reduction to 8 mm fins in Case-SS5 (1 mm thickness) results in more significant performance deterioration with outlet temperature falling to 22.67 °C (9.2 % lower than SS3), though pressure drop decreases substantially to 1.95 Pa (57 % reduction). Temperature contours show progressively less uniform distribution with shorter fins, as they penetrate less into the core flow region. The data demonstrates a clear trade-off: longer, thinner fins provide superior thermal performance but higher pressure penalties, while shorter, thicker fins significantly reduce flow resistance but compromise heat transfer effectiveness.

5.1.3. *Effect of pipe length*

Fig. 10 compares temperature distributions for three cases with identical fin arrangements (32 fins with 16 mm length and 0.5 mm thickness) but varying pipe lengths: 300 mm (Case-SS3), 200 mm (Case-SS6), and 400 mm (Case-SS7). The corresponding performance data for these cases is provided in Table 7. Case-SS3 (300 mm pipe) achieved excellent thermal performance with a 24.97 °C outlet temperature and uniform temperature distribution, but had a pressure drop of 4.54 Pa and pumping power of 0.012267 W. Case-SS6 (200 mm pipe) showed a slight 1.7 % decrease in outlet temperature to 24.55 °C compared to SS3, but had a 21.4 % lower pressure drop of 3.57 Pa and 21.3 % lower pumping power of 0.009648 W. Case-SS7 (400 mm pipe) provided only marginal thermal improvement over SS3, with a 24.89 °C outlet temperature. However, pressure drop increased by 20.0 % to 5.45 Pa, and pumping power rose by 19.9 % to 0.014723 W. So, the shorter 200 mm pipe offered higher thermal performance per unit pressure drop, suggesting better efficiency. However, the 300 mm configuration achieved temperatures closest to the target 25 °C wall condition, which is desirable for energy-efficient building heating. Optimal pipe length selection depends on the specific application needs - whether slightly reduced outlet temperatures are acceptable in exchange for lower pumping power, or maximum thermal recovery is the priority.

5.2. *Transient simulation of the entire storage unit*

This section presents the results and insights gained from investigating the influence of fin configuration, Reynolds number, and inlet air temperature on critical performance metrics such as heat recovery rate, PCM solidification time, and outlet air temperature profile. The transient simulations focused on the entire triple-tube system, including both the PCM domains and the airflow channel.

5.2.1. *Effect of the number of fins in the inner and outer pipes*

Fig. 11 depicts the evolution of temperature contours within the TTHX system over time for different fin configurations (Cases 0–4). At 1200 s, the temperature distributions show significant differences between the cases. In Case 0, with no fins, the temperature gradient across the system is highly non-uniform, indicating poor heat transfer. As the number of fins is increased from Case 1 to Case 4, the temperature contours become progressively more uniform, suggesting enhanced heat transfer between the PCM and the airflow. This trend is particularly evident in the later stages of solidification (3600 and 7200 s), where the higher fin density cases exhibit a more homogeneous temperature field.

Fig. 12 depicts the evolution of liquid-fraction contours within the PCM domain for different fin configurations (Cases 0–4). Fig. 13 provides a more complementary view, presenting the liquid fraction of the PCM along the longitudinal axis of the inner and outer pipes at different time instants. In Case 0, the PCM solidification process is significantly slower, with the inner and outer pipes exhibiting high liquid fractions even at 7200 s. In contrast, the fin-enhanced cases (Cases 1–4) demonstrate a much more rapid solidification, particularly in the inner pipe. By 7200 s, the inner pipe has nearly completed solidification in these cases, while the outer pipe still retains a higher liquid fraction due to its larger PCM mass.

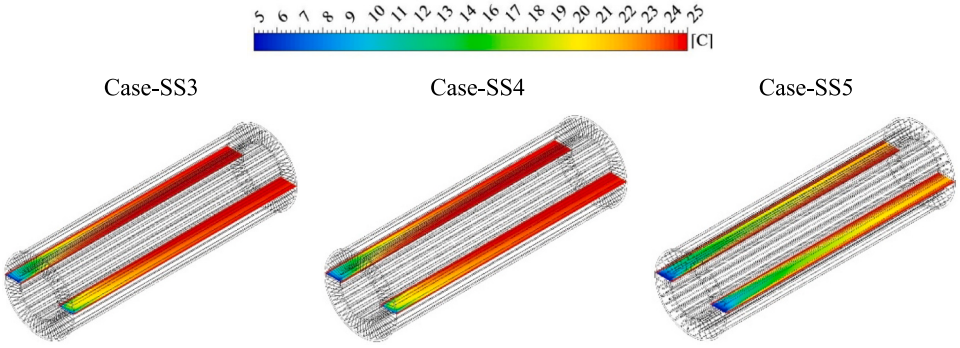

Fig. 9. Temperature distribution contours for varying fin lengths (cases ss3-ss5) with constant number of fins (32) in the TTHX system.

Table 6
Effect of fin length on thermal-hydraulic performance parameters of the TTHX system with 32 fins.

Case	Fin's thickness (mm)	Fin's length (mm)	Number of fins	Pipe length (mm)	Outlet Temperature ($^{\circ}C$)	Mass flow rare (Kg/s)	Pressure drop (Pa)	Pumping power (W)
Case-SS3	0.5	16	32	300	24.9733	0.003313	4.54369	0.012267
Case-SS4	0.6666	12	32	300	23.9294	0.003313	4.54369	0.012267
Case-SS5	1	8	32	300	22.6697	0.003313	1.95226	0.005271

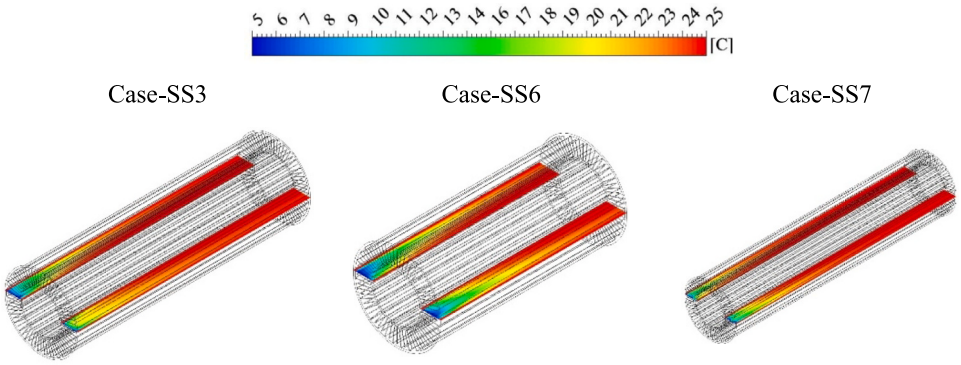

Fig. 10. Temperature distribution contours illustrating the impact of pipe length on air flow in the TTHX system.

Table 7
Effect of pipe length on thermal-hydraulic performance of the TTHX system with 32 fins.

Case	Fin's thickness (mm)	Fin's length (mm)	Number of fins	Pipe length (mm)	Outlet Temperature ($^{\circ}C$)	Mass flow rare (Kg/s)	Pressure drop (Pa)	Pumping power (W)
Case-SS3	0.5	16	32	300	24.9733	0.003313	4.54369	0.012267
Case-SS6	0.5	16	32	200	24.5487	0.003313	3.57359	0.009648
Case-SS7	0.5	16	32	400	24.8940	0.003313	5.45328	0.014723

The accelerated solidification observed when fin density increases, from Case 1 to Case 4, results from the establishment of multiple parallel heat conduction pathways. During solidification, the growing solid PCM layer adjacent to heat transfer surfaces typically creates progressively increasing thermal resistance. The longitudinal fins circumvent this limitation by maintaining direct thermal connections to liquid PCM regions throughout the solidification process. The asymmetric thermal response between inner and outer pipes reflects the fundamental relationship between thermal mass and response time: the inner pipe (0.45 kg PCM) exhibits rapid thermal response due to its smaller thermal capacitance, while the outer pipe (0.87 kg PCM) provides sustained energy release but with slower response characteristics. This thermal decoupling enables the system to provide both rapid initial heating response and prolonged energy delivery, characteristics that are particularly valuable for building heating applications.

Fig. 14 illustrates the solidification time for the PCM in the inner and outer pipes across the various cases. It is observed that the solidification time decreases significantly as the number of fins is increased from Case 0 to Case 4. For the inner pipe, the solidification time is reduced from 11,046 s in Case 0 to 4947 s in Case 4, a 55.3 % improvement. Similarly, the solidification time for the outer pipe decreases from 8858 s in Case 0 to 6823 s in Case 4, a 23.0 % reduction. This trend demonstrates the effectiveness of the increased fin density in enhancing the heat transfer rate from PCM to the airflow, thereby accelerating the solidification process. The data in Fig. 15 further corroborates this finding, showing a corresponding increase in the heat recovery rate as the fin configuration is improved. For the inner pipe, the heat recovery rate increases from 10.05 watts in Case 0 to 21.83 watts in Case 4, a 117.3 % improvement. Likewise, the heat recovery rate for the outer pipe rises from 23.68 watts in Case 0 to 30.66 watts in Case 4, a 29.5 % increase. This significant enhancement in heat recovery rate is directly attributed to the improved heat transfer facilitated by the increased fin surface area and conductive pathways. This indicates that the higher fin density configurations, particularly Case 4, are more effective in extracting thermal energy from the PCM and transferring it to the airflow.

Fig. 16 depicts the evolution of the air outlet temperature over time for various cases. It is observed that the air outlet temperature increases significantly as the number of fins is augmented from Case 0 to Case 4. In Case 0, with no fins, the outlet temperature remains relatively low, reaching a maximum of only around 20 °C towards the end of the 7200-s simulation period. In contrast, Case 4, with the highest fin density, exhibits a much more substantial increase in outlet temperature, reaching nearly 28 °C by the end of the simulation. This trend clearly demonstrates the effectiveness of the enhanced fin configurations in facilitating improved heat transfer from the PCM to the airflow, resulting in a higher-temperature air stream at the outlet. This improved thermal performance is crucial for building heating applications, where the system needs to respond quickly to dynamic heating demands and efficiently utilize the stored thermal energy.

Fig. 17 illustrates the variation of Energy Efficiency Ratio (EER) across different fin configurations (Cases 0–4). Case 0 (non-finned baseline) exhibits the lowest EER of ~2750, highlighting the poor

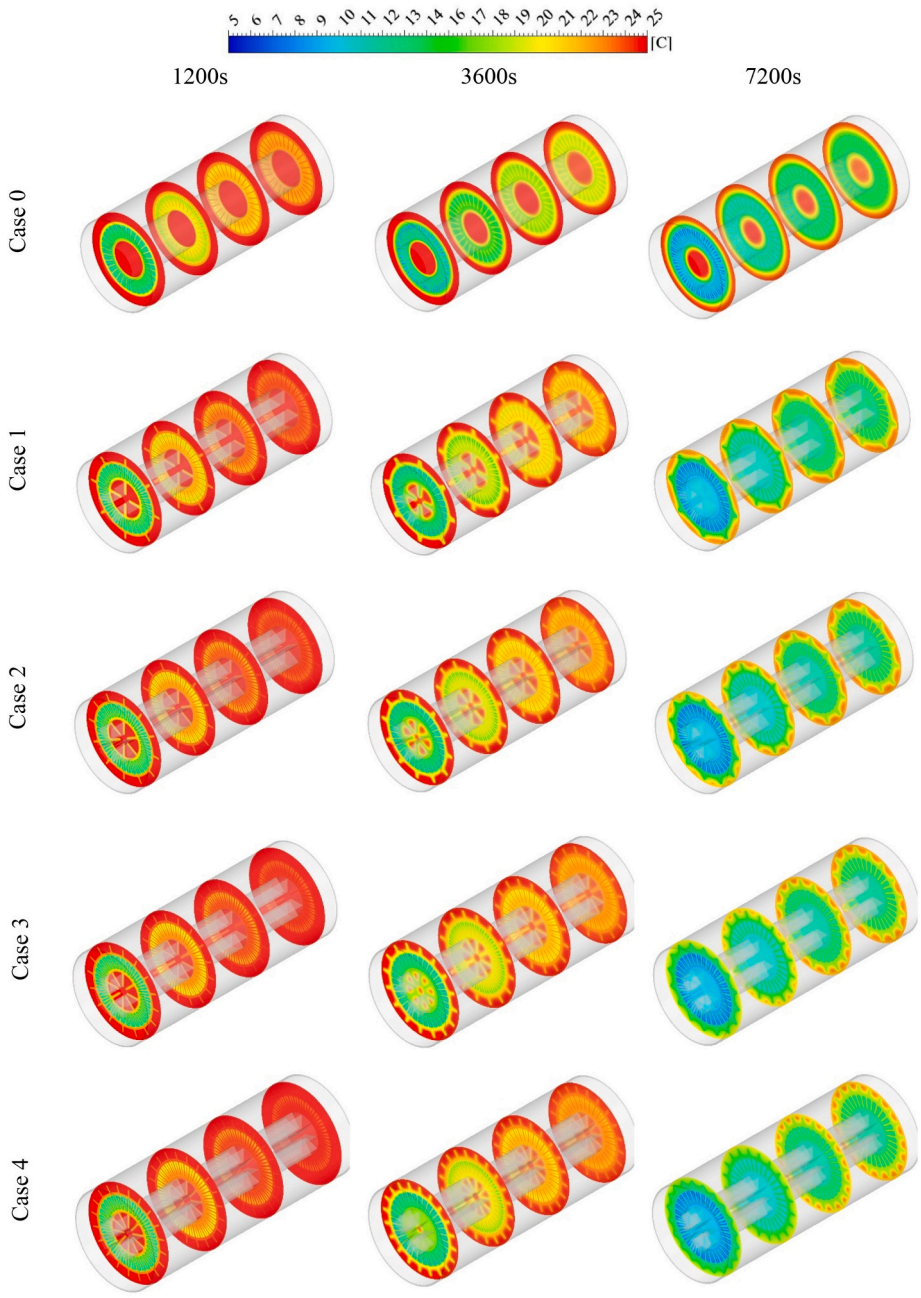

Fig. 11. Temperature contours of PCM along the radial axis of the TTHX system under various fin configurations.

balance between thermal performance and pumping requirements in the absence of extended surfaces. The introduction of fins (Case 1) produces a substantial increase in EER to ~3840, representing a 40 % improvement in system efficiency. Further increases in fin density (Cases 2–4) yield diminishing but still positive gains, with Case 4 achieving the highest EER value of ~4280. The progressive enhancement demonstrates that additional fins continue to improve heat recovery rates at a faster pace than they increase pumping power, up to the optimized threshold investigated in this study.

Fig. 18 provides insights into the solidification behavior of the PCM within the inner and outer pipes. The liquid fraction curves show that the PCM in the inner pipe solidifies at a significantly faster rate compared to the outer pipe, regardless of the fin configuration. This can be attributed to the smaller PCM mass in the inner pipe, which requires less thermal energy to be extracted for complete solidification. However, the fin-enhanced cases, particularly Case 4, exhibit a much more rapid reduction in liquid fraction compared to the non-finned Case 0, highlighting the critical role of the fins in accelerating the solidification process.

Finally, Fig. 19 provides further insights into the temporal evolution of the mean temperatures within the inner pipe, outer pipe, and the air stream. In the fin-enhanced cases, the mean temperature of the PCM in both the inner and outer pipes rises more steeply, indicating a faster heat transfer rate from the PCM to the airflow. Consequently, the air mean temperature also increases more rapidly in these cases, reaching higher values by the end of the simulation period.

5.2.2. Effect of the number of fins on the outer pipe

After identifying Case 4 (10 fins on inner pipe, 20 fins on outer pipe) as the best-performing configuration among Cases 0–4, further investigation was conducted to determine whether additional enhancement could be achieved by increasing the fin density in the outer pipe. Cases 5

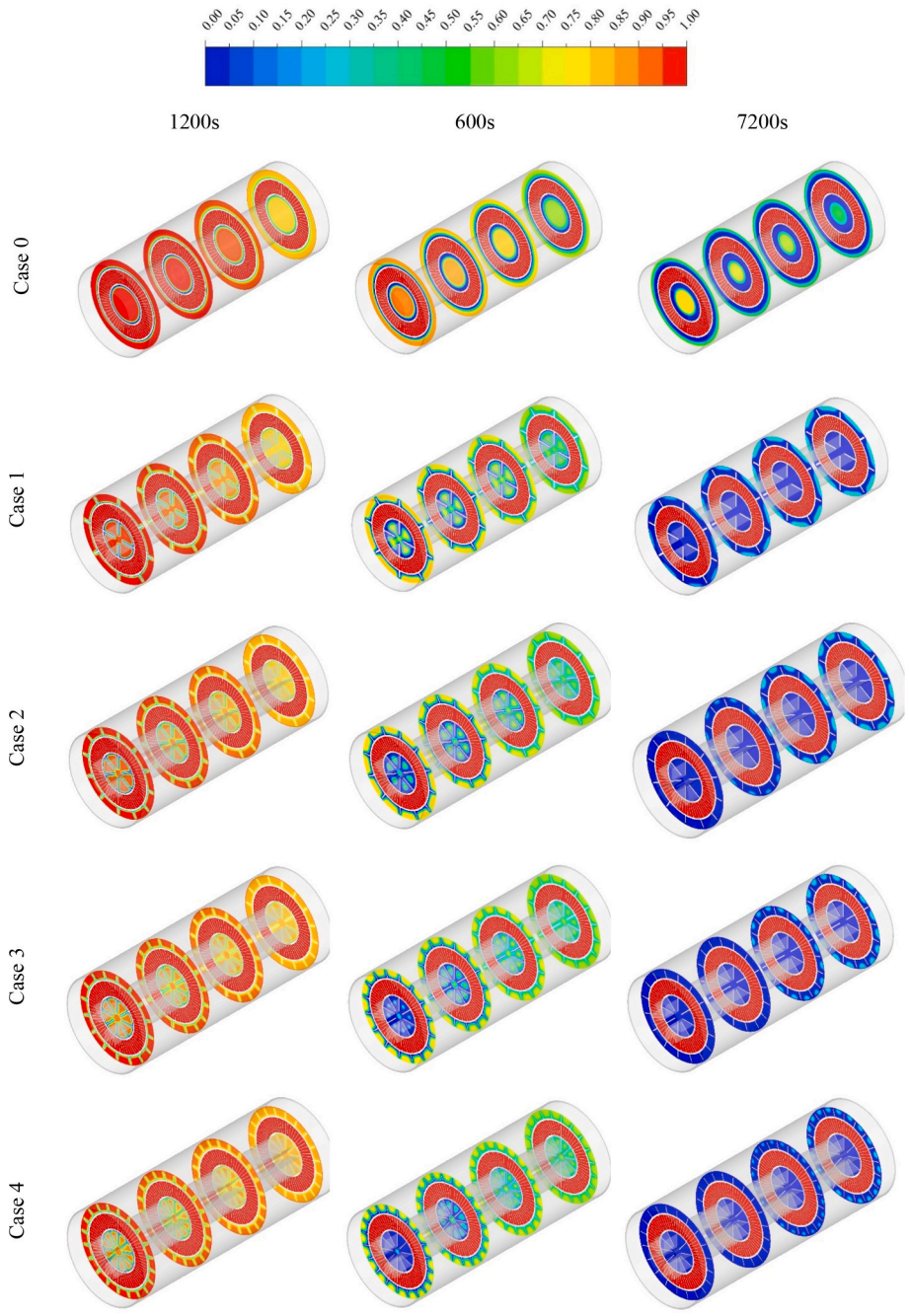

Fig. 12. Evolution of PCM liquid fraction along the radial axis of the TTHX system under various fin configurations.

and 6 were therefore developed, maintaining the inner pipe configuration while incrementally increasing the number of fins on outer pipe to 24 and 28 fins, respectively. Figs. 20 and 21 depict temperature and liquid fraction contours for Cases 5 and 6. Liquid fraction contours in Fig. 20 reveal comparable solidification progression between cases. At 600 s, solid PCM forms near heat transfer surfaces in both configurations. By 7200 s, the inner pipe achieves almost complete solidification in both cases, while the outer pipe retains 20–30 % liquid fraction, with Case 6 showing only marginally better performance despite its additional fins. Temperature distributions in Fig. 21 show nearly identical patterns between the two cases across all time periods. They both exhibit similar temperature gradients from center to periphery, progressing from initial distinct gradients at 600 s to more homogeneous distributions by 7200 s. The minimal differences observed between Cases 5 and 6 indicate that increasing outer pipe fin density from 24 to 28 fins yields diminishing returns in thermal performance. This result suggests an optimization threshold has been reached at 24 fins, beyond which additional fins provide insufficient benefit to justify their inclusion.

Fig. 22 lists solidification times for both inner and outer pipes across the three configurations (Cases 4, 5, and 6). The PCM solidification time remains nearly constant around 5000 s across all three cases in the inner pipe, as expected given the unchanged fin arrangement. For the outer pipe, only modest improvements are observed despite significant fin number increases. Solidification time decreases from 6823 s in Case 4 to 6705 s in Case 5 (a reduction of 1.73 %), and further to 6615 s in Case 6 (representing only a 3.05 % improvement from Case 4). Heat recovery rate data presented in Fig. 23 further substantiates this finding. The inner pipe heat recovery rate remains essentially unchanged around 21.5 watts across all three cases. For the outer pipe, heat recovery increases negligibly from 30.66 watts in Case 4 to 31.20 watts in Case 5 (a

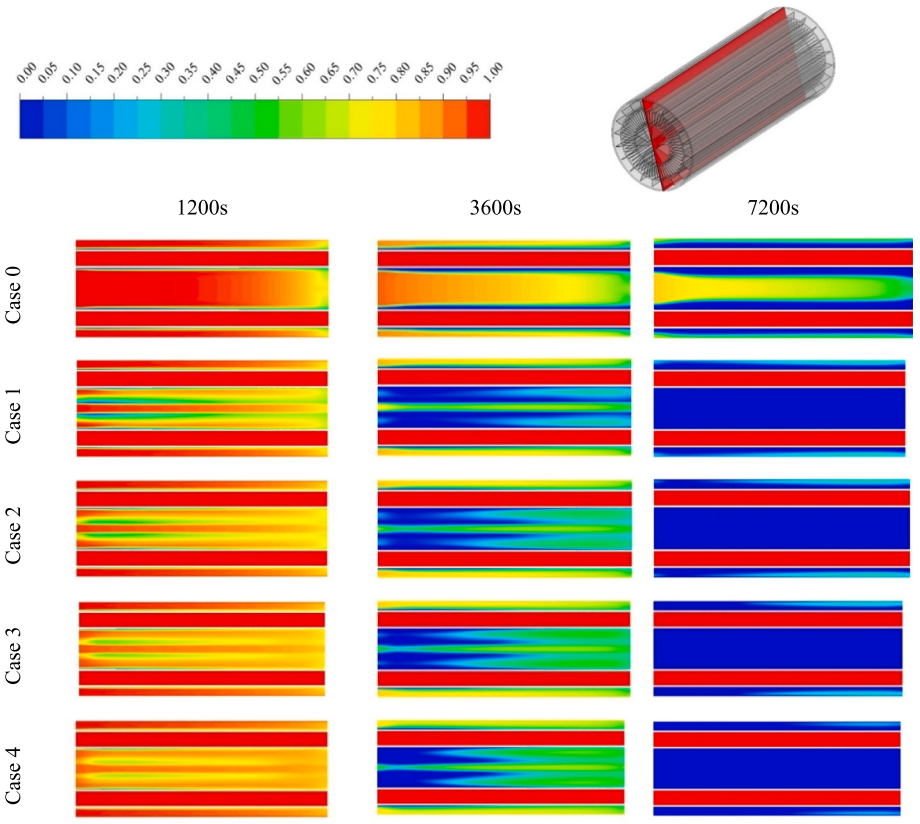

Fig. 13. Liquid fraction of PCM along the longitudinal axis of the inner and outer pipes over time for different fin cases.

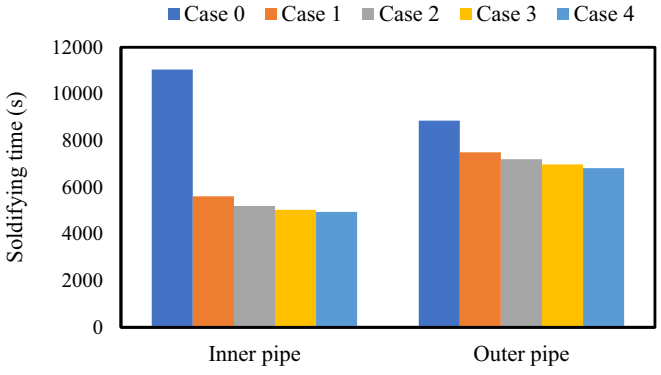

Fig. 14. Comparison of PCM solidification time in the inner and outer pipes across various fin configurations.

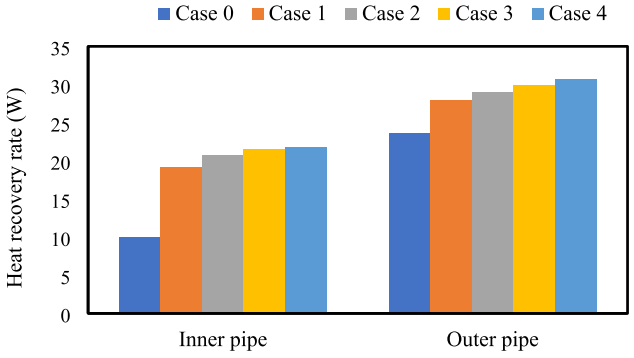

Fig. 15. Comparison of heat recovery rate in the inner and outer pipes across various fin configurations.

1.7 % improvement), and to 31.63 watts in Case 6 (only a 3.1 % increase compared to Case 4). These marginal enhancements fail to justify the additional material and manufacturing complexity introduced by the extra fins.

The temporal evolution of air outlet temperature shown in Fig. 24 confirms the limited practical impact of additional fins. The three curves tracking outlet air temperature over the 7200-s simulation period are virtually indistinguishable, with all cases achieving peak temperatures of approximately 28 °C. The magnified inset between 3600 and 5400 s shows temperature differences of less than 0.1 °C between cases. This finding suggests that resources would be better allocated to alternative enhancement approaches rather than increasing fin density beyond the established threshold. The temporal evolution of air outlet temperature shown in Fig. 24 confirms the limited practical impact of additional fins. The three curves tracking outlet air temperature over the 7200-s simulation period are virtually indistinguishable, with all cases achieving peak temperatures of approximately 28 °C. The magnified inset between 3600 and 5400 s shows temperature differences of less than 0.1 °C between cases. This finding suggests that resources would be better allocated to alternative enhancement approaches rather than increasing fin density beyond the established threshold. From a purely thermal performance perspective, Case 6 (28 fins) achieves the highest performance within the parameter space investigated. However, the marginal 3 % improvement over Case 5 (24 fins) might not justify the additional manufacturing complexity and cost. Therefore, further analysis (beyond the scope of this study) considering factors such as manufacturing costs and assembly complexity alongside thermal performance metrics is required to establish the optimal configuration.

Fig. 25 compares EER of the optimized fin configurations (Cases 4–6). A clear upward trend is observed with increasing fin density in the outer pipe. Case 4 records the lowest EER of ~4280, while Case 5

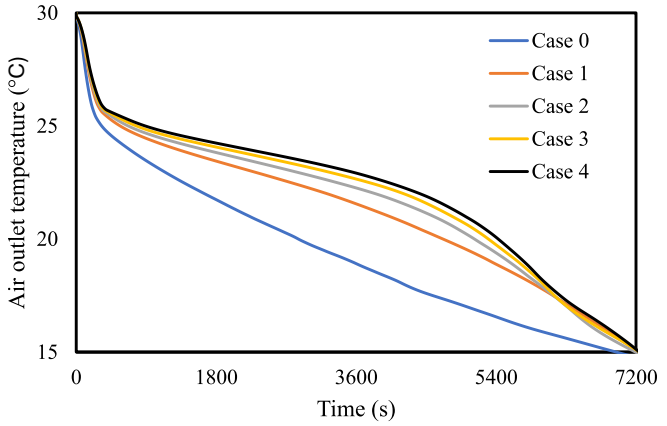

Fig. 16. Evolution of air outlet temperature during PCM solidification under various fin configurations.

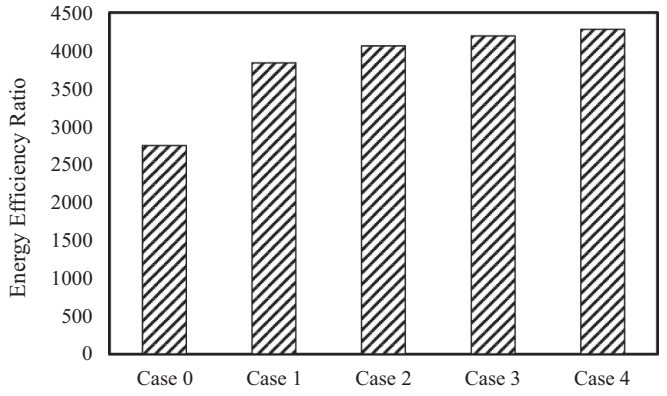

Fig. 17. Evolution of EER for various fin configurations.

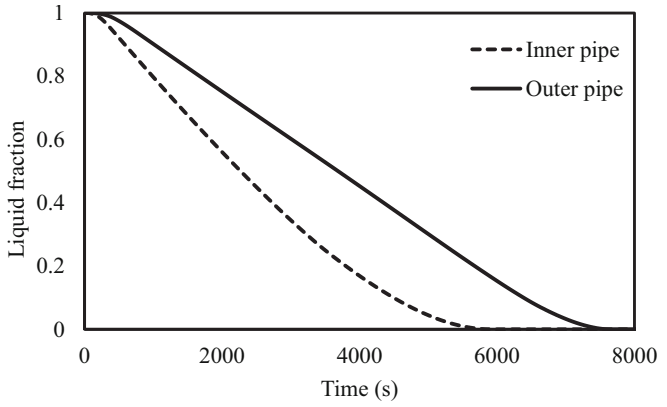

Fig. 18. Temporal evolution of PCM liquid fraction during solidification in the inner and outer pipes under various fin configurations.

achieves a moderate increase to 4302, and Case 6 reaches the maximum value of around 4320. Although the absolute improvements between successive cases are relatively small (less than 1 % increase from Case 4 to Case 6), they confirm that additional fins in the outer pipe continue to enhance overall energy efficiency by improving heat recovery at a faster rate than the associated pumping power penalty. Importantly, the marginal gain from Case 5 to Case 6 suggests that the system is approaching a practical optimization threshold, beyond which further increases in fin number may not justify the added manufacturing complexity and cost. This observation aligns with the earlier thermal

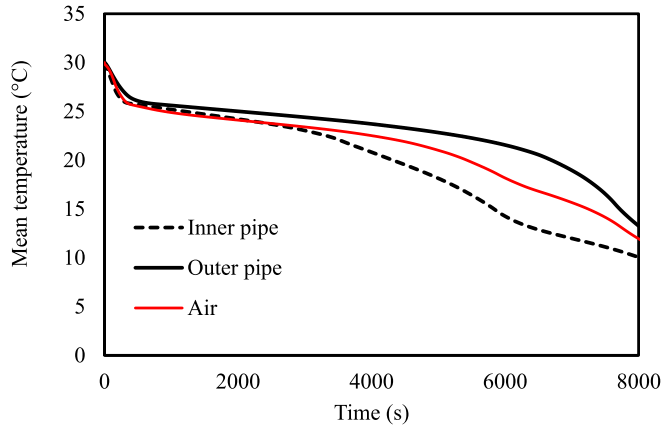

Fig. 19. Temporal evolution of mean temperatures in the inner pipe, outer pipe, and air stream during PCM solidification under various fin configurations.

analysis, reinforcing that Case 6 represents the most efficient design within the investigated parameter space.

5.2.3. *Effect of Reynolds number*

In this section, the effect of Reynolds number variation on the thermal performance of the TTHX system is investigated using Case 6 configuration, which was previously identified as the optimal fin arrangement. Reynolds number directly affects the convective heat transfer at the air-PCM interface, thereby influencing solidification rates, heat recovery efficiency, and outlet air temperature profiles. Fig. 26 provides visual comparison through liquid-fraction contours across different Reynolds numbers ($Re = 500$ and $Re = 1000$). At Re = 500, the PCM solidification process progresses slowly, with substantial liquid fractions remaining at 3600 s, especially in the outer pipe region. By 7200 s, significant portions of PCM remain in liquid state, particularly in the outer annular space. The $Re = 1000$ case exhibits markedly accelerated solidification patterns. At 1200s, solid layers around heat transfer surfaces are noticeably thicker compared to Re = 500. By 3600 s, approximately half of the PCM has solidified in both annular spaces, and at 7200 s, solidification is substantially more advanced throughout the system, with only small pockets of liquid PCM remaining in the outer annular space.

Fig. 27 reveal significant variations in the temperature distribution contours. At Re = 500, the temperature gradients appear more pronounced and less uniform throughout the system. The core regions maintain higher temperatures for longer periods, particularly at 3600 s, indicating slower heat transfer from PCM to the airflow. In contrast, at Re = 1000, more uniform temperature distributions are observed with accelerated cooling patterns. By 3600 s, the $Re = 1000$ case shows notably lower temperatures across the entire cross-section compared to $Re = 500$, suggesting enhanced heat extraction. At 7200 s, this difference becomes more pronounced, with Re = 1000 demonstrating significantly more advanced cooling throughout the system. This improved performance at higher Reynolds numbers suggests that the system's thermal response can be significantly enhanced by increasing the airflow rate, though this would need to be balanced against the higher pumping power requirements that naturally accompany increased flow rates.

In Fig. 28, the temporal evolution of PCM liquid fraction is distinctly influenced by Reynolds numbers in both the inner and outer pipes. In the inner pipe (Fig. 28a), complete solidification (liquid fraction <0.05) is achieved in about 6000 s at Re = 2000, and 10,500 s at Re = 1000. This represents a 42.9 % reduction in solidification time when Reynolds number is doubled from 1000 to 2000. Similar trends are observed in the outer pipe (Fig. 28b), where the solidification time is reduced from approximately 13,000 s at $Re = 1000$, and 7000 s at $Re = 2000$ (46.2 % additional reduction). The progressively diminishing percentage

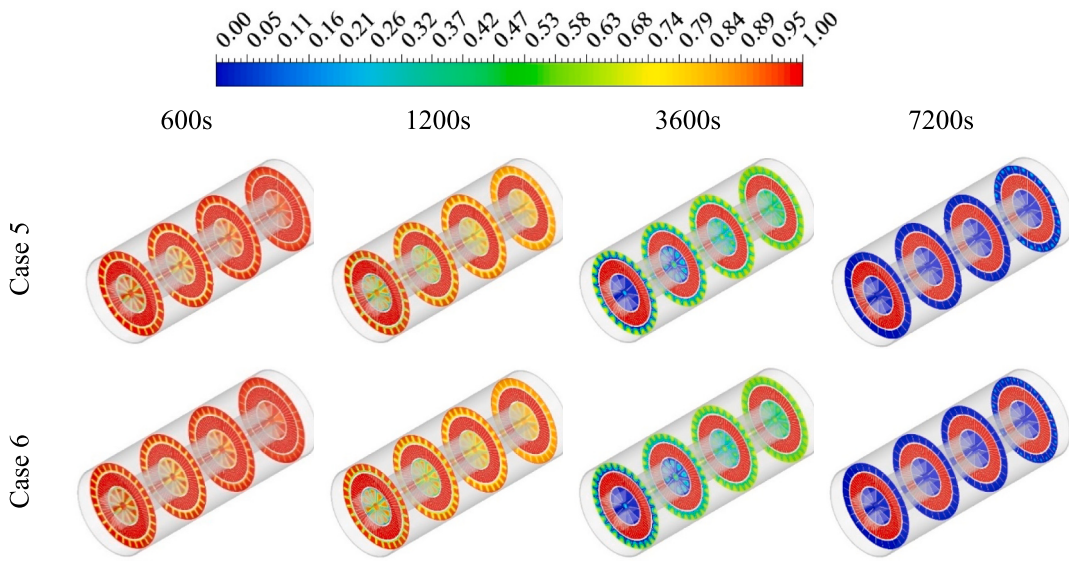

Fig. 20. Evolution of PCM liquid fraction contours along the radial axis over different operation times for fin configurations Case 5 (24 fins) and Case 6 (28 fins).

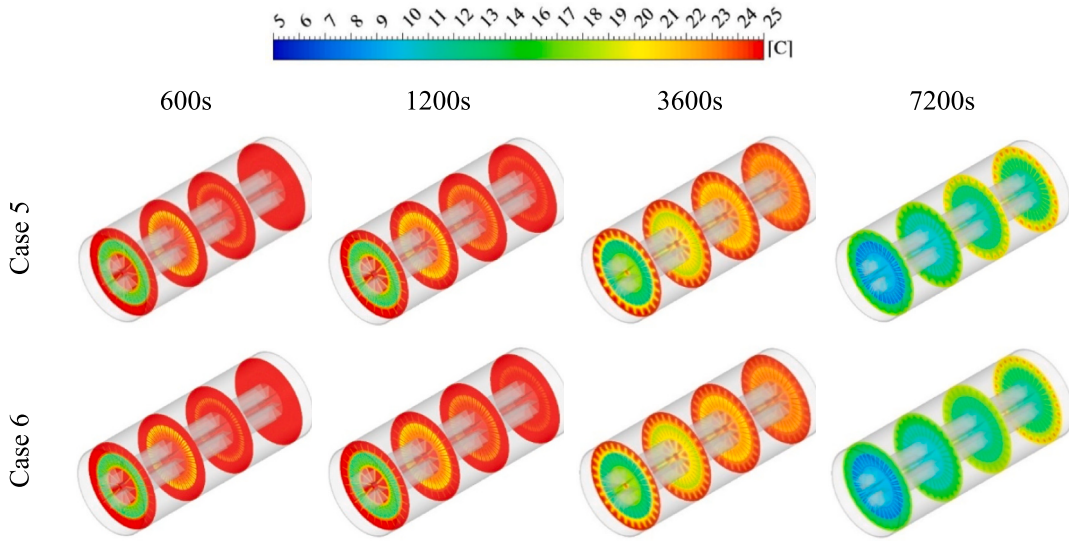

Fig. 21. Temperature distribution contours along the radial axis over different operation times for fin configurations Case 5 (24 fins) and Case 6 (28 fins).

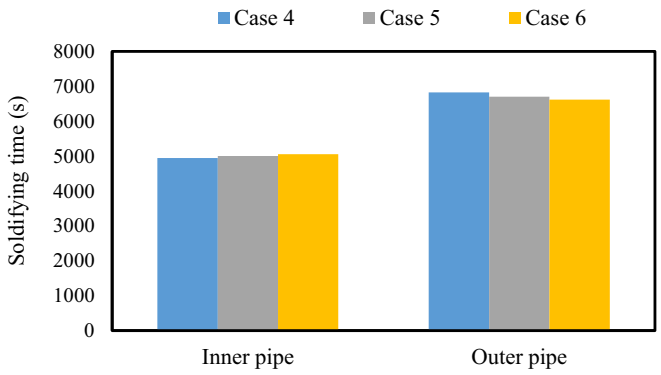

Fig. 22. Comparison of PCM solidification time in the inner pipe (10 fins) and outer pipe for Cases 4 (20 fins), 5 (24 fins), and 6 (28 fins).

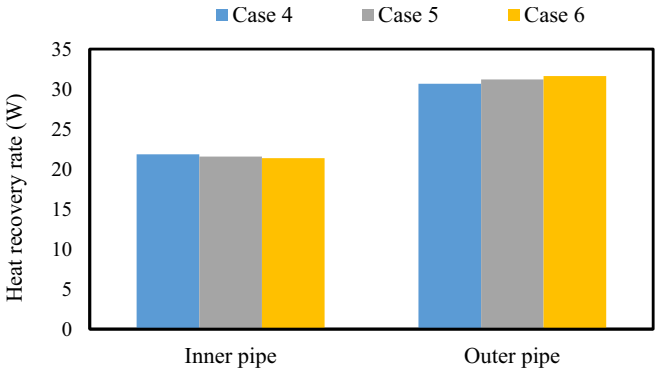

Fig. 23. Comparison of PCM heat recovery rate in the inner pipe (10 fins) and outer pipe for Cases 4 (20 fins), 5 (24 fins), and 6 (28 fins).

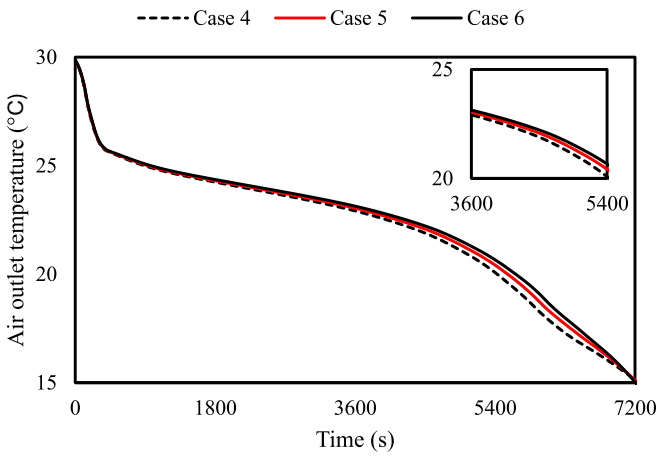

Fig. 24. Temporal evolution of air outlet temperature over 7200 s of PCM solidification for Cases 4, 5, and 6.

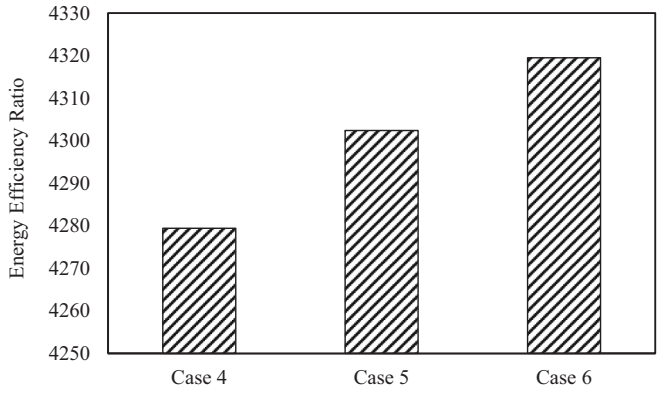

Fig. 25. Evolution of EER for Cases 4, 5 and 6.

improvement suggests that performance enhancement begins to plateau at higher Reynolds numbers, particularly in the outer pipe.

The heat recovery rate data presented in Fig. 29 demonstrates a strong positive correlation with Reynolds number in both PCM compartments. In the inner pipe, heat recovery rates of approximately 6.1 W, 12.2 W, and 21.3 W are observed at Re = 500, 1000, and 2000 respectively, showing a 45.5 % increase when Reynolds number is doubled from 500 to 1000, and a further 37.5 % increase when doubled from 1000 to 2000. For the outer pipe, heat recovery rates increase from approximately 8.2 W at *Re* = 500 to 16.4 W at *Re* = 1000 (53.3 % increase), and to 31.6 W at *Re* = 2000 (39.1 % increase). The total system heat recovery is enhanced by 113 % when Reynolds number is increased from 500 to 2000, highlighting the substantial impact of airflow rate on thermal performance.

Fig. 30 illustrates how Reynolds number affects the temporal evolution of air outlet temperature during the PCM discharge process. At Re = 500, the outlet temperature reaches a peak of approximately 28 °C and maintains relatively high temperatures (above 25 °C) for nearly 10,000 s before gradually declining. As Reynolds' number increases to 1000 and 2000, maximum outlet temperatures decrease to approximately 26 °C and 24 °C, respectively. However, the curves for higher Reynolds numbers exhibit steeper initial rises and earlier peaks, demonstrating faster thermal response.

In conclusion, higher Reynolds numbers significantly enhance heat transfer rates and reduce solidification times, allowing more rapid system responsiveness to dynamic heating demands. However, this comes at the cost of reduced outlet air temperatures, which may impact thermal comfort in building heating applications. The 113 % improvement in overall heat recovery rate when increasing Reynolds number from 500 to 2000 must be balanced against the approximately 14.3 % reduction in peak outlet temperature (from 28 °C to 24 °C). These findings suggest that optimal Reynolds number selection depends on specific application requirements. For applications requiring rapid thermal response and high total energy transfer, higher Reynolds numbers would be preferred. For applications where maintaining elevated outlet temperatures is prioritized over quick response times, lower Reynolds numbers may be more appropriate.

Fig. 31 illustrates the variation of EER with Reynolds number for the optimized finned configuration. At Re = 500, the EER is ~1168, indicating limited heat recovery relative to pumping power. As the Reynolds number increases to 1000, the EER more than doubles to around 2334, reflecting the enhanced convective heat transfer that significantly accelerates PCM solidification and boosts overall heat recovery. At Re = 2000, the EER reaches its maximum value of about 4320, representing nearly a fourfold improvement over Re = 500. These results demonstrate that increasing airflow enhances thermal performance at a faster

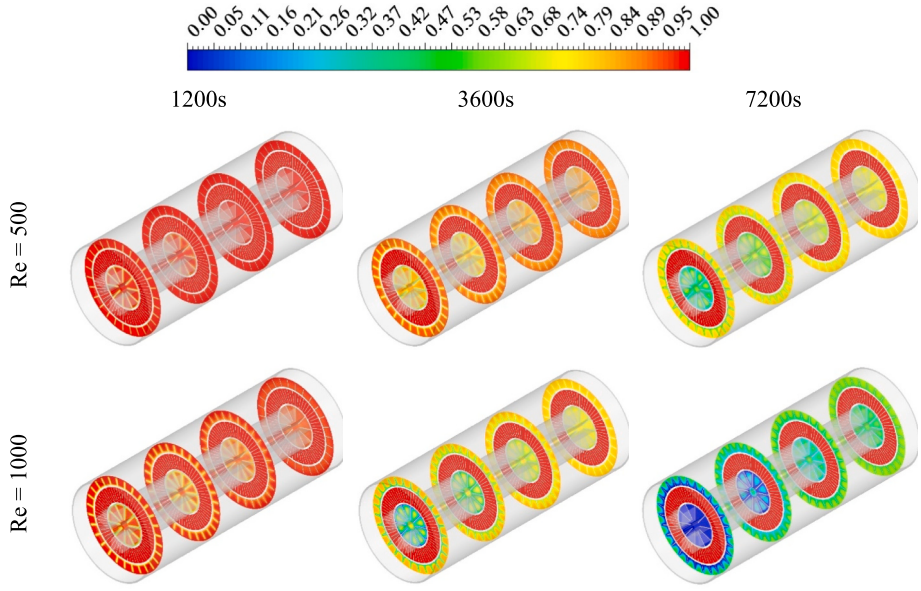

Fig. 26. Liquid-fraction contours at different solidification periods comparing Reynolds numbers of 500 and 1000 in the Case 6 configuration.

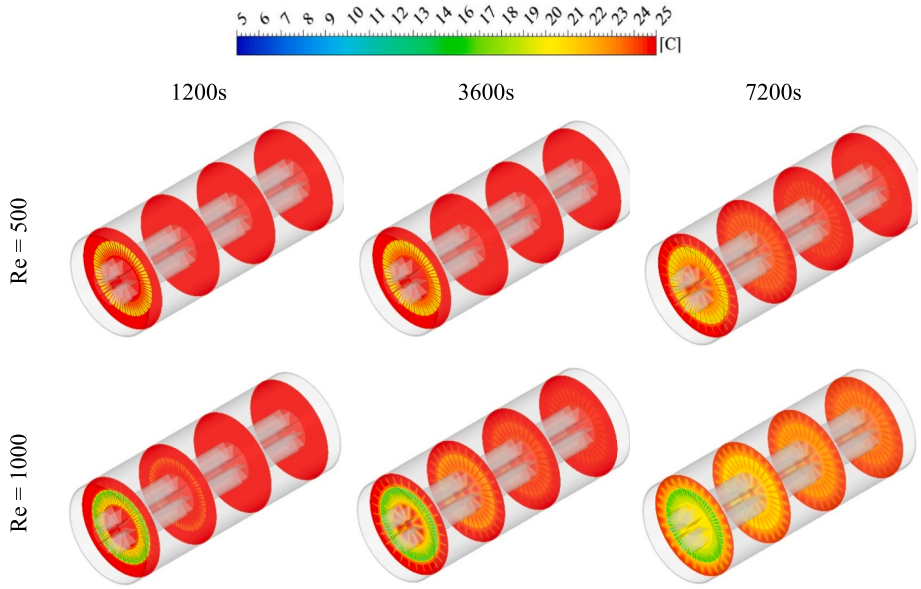

Fig. 27. Temperature distribution contours at different solidification periods comparing Reynolds numbers of 500 and 1000 in the Case 6 configuration.

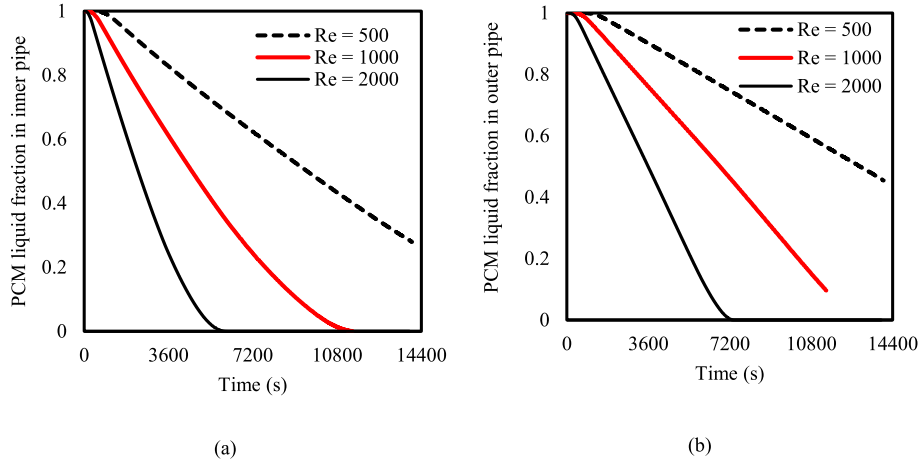

Fig. 28. Temporal evolution of PCM liquid fraction during solidification: (a) inner pipe and (b) outer pipe under Reynolds numbers of 500, 1000, and 2000.

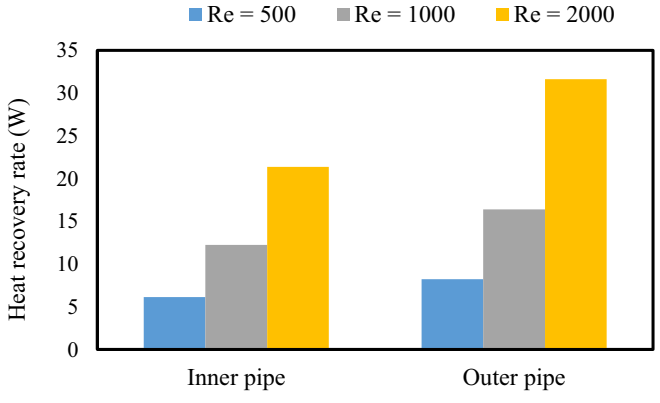

Fig. 29. Effect of Reynolds numbers (500, 1000, and 2000) on heat recovery rates in the inner and outer pipes of the Case 6 configuration.

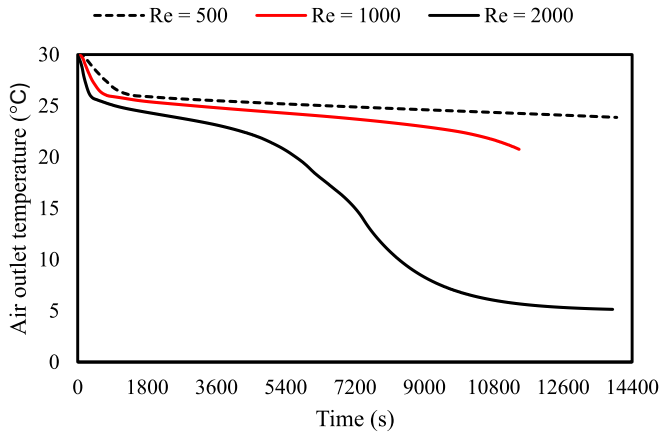

Fig. 30. Air outlet temperature profiles over 14,400 s solidification period for Reynolds numbers of 500, 1000, and 2000.

rate than the corresponding rise in pumping power, thereby improving system-level efficiency. However, it should be noted that higher Reynolds numbers also reduce peak outlet temperature due to faster heat

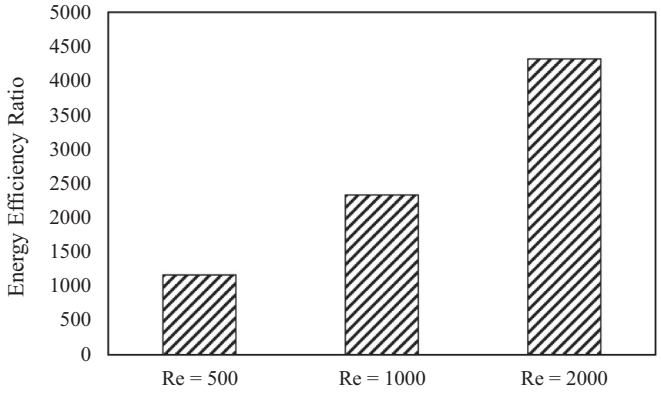

Fig. 31. Evolution of EER for Reynolds numbers of 500, 1000, and 2000 (case 6).

extraction, as discussed earlier. Therefore, the optimal Reynolds number must be chosen based on the trade-off between maximizing energy efficiency and maintaining adequate outlet air temperature for thermal comfort in building applications.

5.2.4. *Effect of air inlet temperature*

This section explores how variations in air inlet temperature affect the solidification behavior and overall thermal performance of the optimized Case 6 configuration. Three different inlet air temperatures (0 °C, 5 °C, and 10 °C) were examined to understand the system's responsiveness under varying operational requirements. The liquid fraction contours in Fig. 32 show significant differences in thermal behavior of the PCM domain. At 1200s, the PCM solidification with 0 °C inlet air shows markedly thicker solid layers developing around the heat transfer surfaces compared to the 10 °C case. By 3600 s, approximately 60–70 % of the PCM has solidified with 0 °C inlet air, whereas the 10 °C case exhibits only about 40–50 % solidification. At the final time point (7200 s), the 0 °C inlet air case displays near-complete solidification across both PCM compartments with only small liquid pockets remaining in the outer annular space, while the 10 °C case still retains significant liquid PCM, particularly in the outer tube.

Fig. 33 further substantiates these observations through temperature distribution contours. At 1200s, the system with 0 °C inlet air demonstrates considerably steeper temperature gradients compared to the 10 °C case. These more pronounced gradients persist throughout the simulation duration, indicating enhanced thermal driving force with the lower inlet temperature. By 7200 s, the overall system temperature with 0 °C inlet air falls substantially below that of the 10 °C case, with noticeably cooler regions extending throughout both PCM domains in the inner and outer pipe. This analysis confirms that lower inlet air temperature provides a greater temperature differential between the PCM and airflow, accelerating the heat transfer rate and consequently the solidification process. This parameter fundamentally determines the system's thermal behavior and operational response time.

Fig. 34 illustrates the temporal evolution of PCM liquid fraction in both the inner pipe (29a) and outer pipe (29b) at three different inlet air temperatures (0 °C, 5 °C, and 10 °C). In the inner pipe, complete solidification (liquid fraction <0.05) is achieved in 4400 s, 6000 s, and 7500 s for inlet temperatures of 0 °C, 5 °C, and 10 °C, respectively. This represents a 26.7 % reduction in solidification time when the inlet temperature is decreased from 5 °C to 0 °C, and a 25.0 % increase when raised from 5 °C to 10 °C. Similar trends are observed in the outer pipe, where solidification times are extended to approximately 5800 s, 7100 s, and 9300 s for the respective inlet temperatures. This corresponds to an 18.3 % reduction when inlet temperature decreases from 5 °C to 0 °C and a 31.0 % increase when raised from 5 °C to 10 °C.

Fig. 35 quantifies the heat recovery rates for both PCM compartments across the three inlet temperature conditions. For the inner pipe, heat recovery rates of approximately 26.7, 21.3, and 15.7 W are recorded at inlet temperatures of 0, 5, and 10 °C, respectively. This represents a 25.4 % increase in heat recovery when inlet temperature is reduced from 5 °C to 0 °C, and a 26.3 % decrease when raised from 5 °C to 10 °C. The outer pipe exhibits a similar pattern with heat recovery rates of 39.3 W, 31.6 W, and 23.7 W for the respective inlet temperatures. This represents a 24.4 % increase when inlet temperature decreases from 5 °C to 0 °C and a 25.0 % decrease when raised from 5 °C to 10 °C. The entire system heat recovery is enhanced by 24.7 % when inlet temperature is decreased from 5 °C to 0 °C, and reduced by 25.5 % when increased from 5 °C to 10 °C.

Fig. 36 depicts the temporal evolution of air outlet temperature during the PCM discharge mode. With 0 °C inlet air, the outlet temperature reaches a peak around 19 °C before gradually declining. At 5 °C inlet temperature, the maximum outlet temperature increases to approximately 24 °C, while the 10 °C case achieves nearly 28 °C. The temperature rise (difference between inlet and outlet temperatures) is calculated to be approximately 19 °C, 19 °C, and 18 °C for the 0 °C, 5 °C,

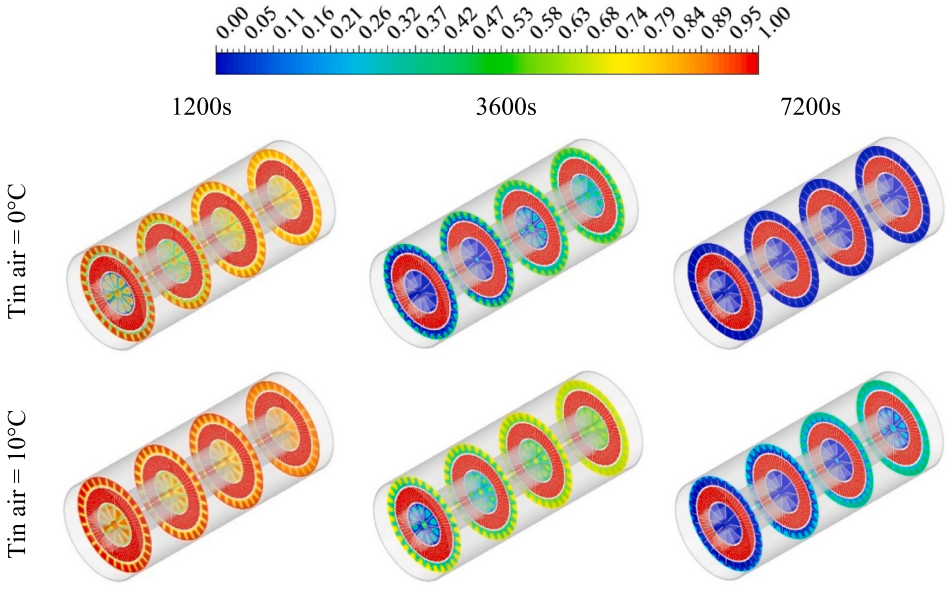

Fig. 32. PCM liquid fraction contours at different solidification intervals comparing inlet air temperatures of 0 °C and 10 °C in the Case 6 configuration.

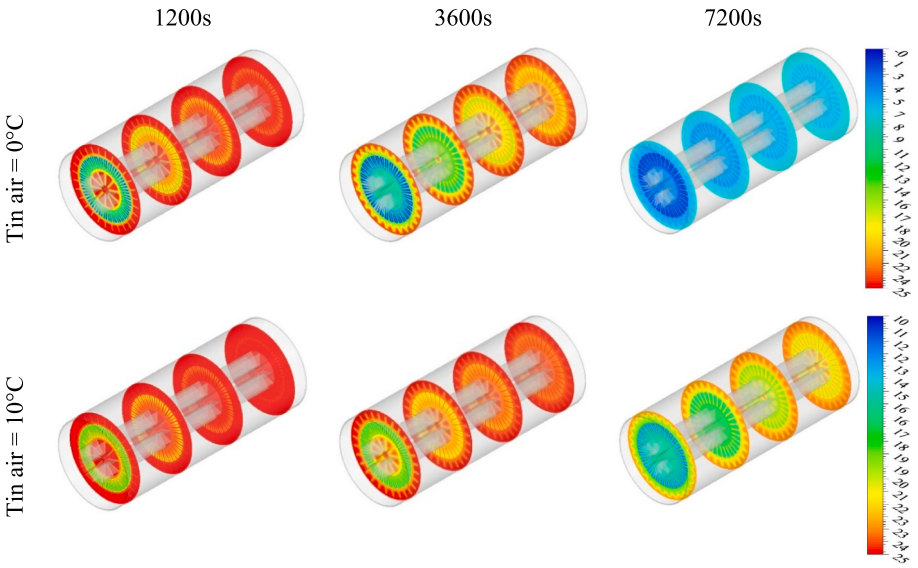

Fig. 33. Temperature distribution contours at different solidification intervals comparing inlet air temperatures of 0 °C and 10 °C in the Case 6 configuration.

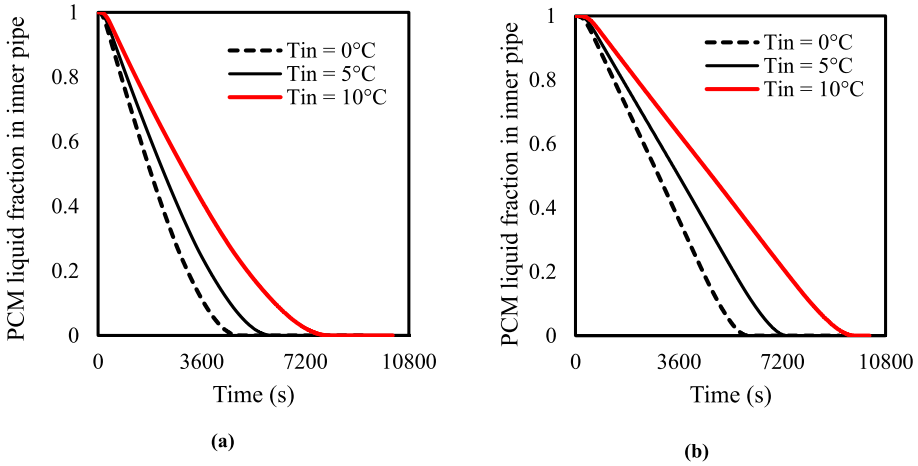

Fig. 34. Effect of inlet air temperature on PCM liquid fraction evolution: (a) inner pipe and (b) outer pipe in the Case 6 configuration.

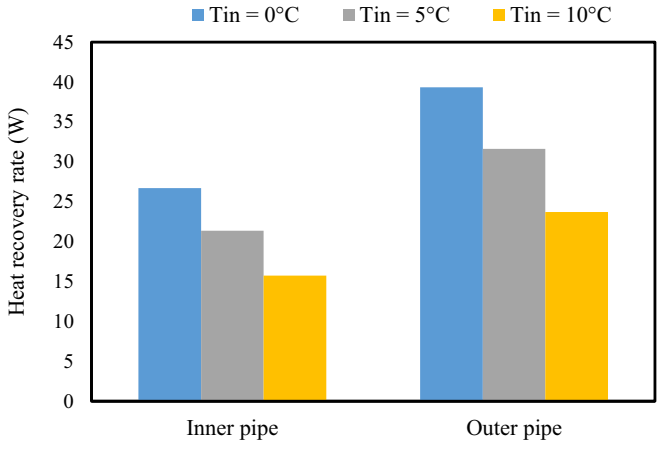

Fig. 35. Comparison of PCM heat recovery rates in the inner and outer pipes under inlet air temperatures of 0 °C, 5 °C, and 10 °C in the Case 6 configuration.

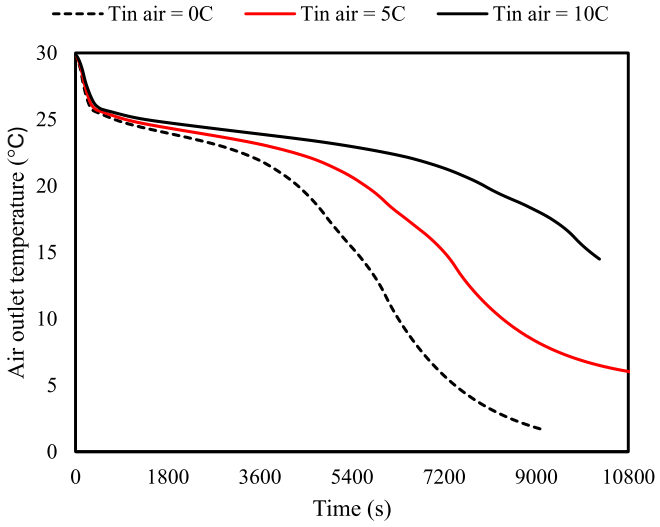

Fig. 36. Temporal profiles of air outlet temperatures over 10,800 s for inlet temperatures of 0 °C, 5 °C, and 10 °C.

and 10 °C cases respectively, indicating that the heat transfer effectiveness remains relatively consistent across different inlet conditions.

From these results, a fundamental trade-off is identified between thermal responsiveness and outlet temperature suitability. Lower inlet air temperatures significantly enhance heat transfer rates and reduce solidification times, allowing more rapid response to dynamic heating demands. However, this comes at the cost of reduced outlet air temperatures, which may fail to meet thermal comfort requirements in certain building heating applications. The optimal inlet temperature selection therefore depends on specific application requirements, balancing the need for rapid thermal response with appropriate supply air temperatures for occupant comfort.

Fig. 37 presents EER for three inlet air temperatures (0 °C, 5 °C, and 10 °C). A clear decreasing trend is observed as the inlet air temperature increases. At Tin = 0 °C, the system achieves the highest EER, reflecting the strong thermal driving force between the cold air stream and the PCM, which accelerates solidification and increases heat recovery relative to the required pumping power. When the inlet temperature rises to 5 °C, the EER decreases, representing a 20 % reduction in efficiency. A further increase to Tin = 10 °C reduces the EER, showing that the system becomes progressively less efficient as the thermal gradient weakens. These results demonstrate that lower inlet temperatures substantially enhance energy efficiency by maximizing heat extraction for a given pumping power. However, higher inlet temperatures, while less efficient in terms of EER, deliver warmer outlet air streams, which may be preferable in certain building heating applications where occupant comfort requires higher supply temperatures. Thus, selecting the appropriate inlet temperature involves balancing efficiency gains with the thermal comfort requirements of the application.

6. Conclusion

This study has numerically investigated the design optimization and performance enhancement of a novel triplex-tube PCM-to-air heat exchanger with longitudinal fins for building heating applications. The following key findings have been established:

(1) From a practical implementation perspective, the steady-state analysis identified that 32 fins with 16 mm length represents an optimal configuration balancing thermal performance with acceptable pressure drop.
(2) The optimal fin configuration (10 on the inner pipe, 28 on the outer) reduced the solidification time by 55.3 % for the inner pipe and 23.0 % for the outer pipe compared to the non-finned design.
(3) Increasing the Reynolds number from 500 to 2000 boosts the heat recovery rate by 113 %. However, this comes at the cost of a trade-off: the peak outlet air temperature drops from 28 °C to 24 °C, which may affect occupant comfort.
(4) Decreasing inlet temperature from 5 °C to 0 °C enhanced total heat recovery by 24.7 % and reduced solidification time by approximately 25 %, while increasing inlet temperature to 10 °C decreased heat recovery by 25.5 % and extended solidification time by about 28 %.
(5) Optimized fin configurations, higher Reynolds numbers, and lower inlet temperatures consistently improved the Energy Efficiency Ratio (EER). With a maximum EER of over 5000, the triplex-tube PCM-to-air heat exchanger demonstrates superior thermal–hydraulic efficiency.

These numerical findings effectively address the challenges of energy efficiency for PCM-based heating systems in buildings. Future work should focus on experimental validation of these numerical findings, long-term cycling performance assessment, and techno-economic analysis to further support the commercial viability of this promising technology for sustainable building applications.

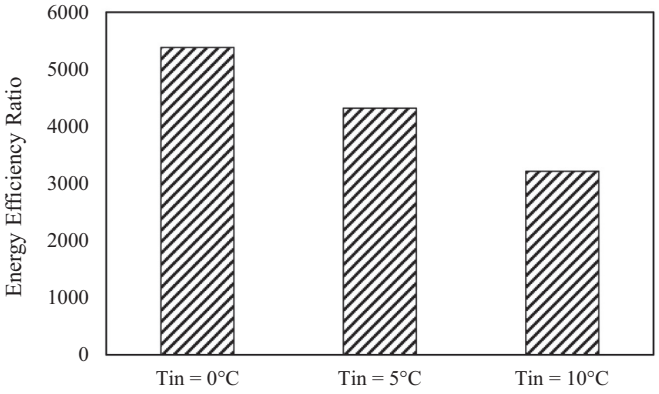

Fig. 37. Evolution of EER for inlet temperatures of 0 °C, 5 °C, and 10 °C (case 6).

CRediT authorship contribution statement

Mohamed Ahmed Said: Writing – original draft, Methodology, Investigation, Conceptualization. **Jasim M. Mahdi:** Writing – original draft, Investigation, Formal analysis, Conceptualization. **Marrwa S. Ghanim:** Writing – original draft, Visualization, Validation, Software. **Khalil Hajlaoui:** Writing – original draft, Supervision, Data curation, Conceptualization. **Nashmi H. Alrasheedi:** Writing – original draft, Resources, Funding acquisition, Formal analysis. **Mohammad Ghalambaz:** Writing – review & editing, Writing – original draft, Software, Resources. **Pouyan Talebidadehsardari:** Writing – review & editing, Writing – original draft, Visualization, Software, Project administration. **Nidhal Ben Khedher:** Writing – original draft, Methodology, Formal analysis, Data curation.

Declaration of competing interest

The authors clarify that there is no conflict of interest for report.

Acknowledgement

This work was supported and funded by the Deanship of Scientific Research at Imam Mohammad Ibn Saud Islamic University (IMSIU) (grant number IMSIU-DDRSP-RP25).

Data availability

Data will be made available on request.

References

[1] D. Ürge-Vorsatz, L.F. Cabeza, S. Serrano, C. Barreneche, K. Petrichenko, Heating and cooling energy trends and drivers in buildings, Renew. Sust. Energ. Rev. 41 (2015) 85–98.
[2] M. Khalil, A.S. McGough, Z. Pourmirza, M. Pazhoohesh, S. Walker, Machine learning, deep learning and statistical analysis for forecasting building energy consumption — a systematic review, Eng. Appl. Artif. Intell. 115 (2022) 105287.
[3] IRENA, Innovation Outlook: Thermal Energy Storage, International Renewable Energy Agency, Abu Dhabi, 2020.
[4] M. Saffari, A. de Gracia, S. Ushak, L.F. Cabeza, Passive cooling of buildings with phase change materials using whole-building energy simulation tools: a review, Renew. Sust. Energ. Rev. 80 (2017) 1239–1255.
[5] I.A. Laasri, N. Es-sakali, A. Outzourhit, M.O. Mghazli, Evaluation of phase change materials for a light-weight building in Morocco: effect of building's volume, window orientation & infiltration, Energ. Built. Environ. 5 (2024) 863–877.
[6] J.M. Mahdi, S. Lohrasbi, E.C. Nsofor, Hybrid heat transfer enhancement for latent-heat thermal energy storage systems: a review, Int. J. Heat Mass Transf. 137 (2019) 630–649.
[7] H. Jouhara, A. Żabnieńska-Góra, N. Khordehgah, D. Ahmad, T. Lipinski, Latent thermal energy storage technologies and applications: a review, Int. J. Thermofluids. 5-6 (2020) 100039.
[8] G. Gholamibozanjani, M. Farid, Application of an active PCM storage system into a building for heating/cooling load reduction, Energy 210 (2020) 118572.

[9] H. Yin, A. Norouziasas, M. Hamdy, PCM as an energy flexibility asset: how design and operation can be optimized for heating in residential buildings? Energ. Build. 322 (2024) 114721.
[10] H. Wang, Z. Xiao, Z. Hou, Y. Zhang, Q. Shi, X. Ye, Binary decanoic acid-paraffin composite PCMs in expanded perlite and passive temperature control in building envelopes, Appl. Therm. Eng. 278 (2025) 127212.
[11] A. Torres-Rodríguez, D. Morillón-Gálvez, D. Aldama-Ávalos, V.H. Hernández-Gómez, Kerdan I. García, Thermal performance evaluation of a passive building wall with CO2-filled transparent thermal insulation and paraffin-based PCM, Sol. Energy 205 (2020) 1–11.
[12] A. Sharma, V.V. Tyagi, C.R. Chen, D. Buddhi, Review on thermal energy storage with phase change materials and applications, Renew. Sust. Energ. Rev. 13 (2009) 318–345.
[13] N. Sarier, E. Onder, Organic phase change materials and their textile applications: an overview, Thermochim. Acta 540 (2012) 7–60.
[14] A. Yadav, A. Pandey, M. Samykano, B. Kalidasan, Z. Said, A review of organic phase change materials and their adaptation for thermal energy storage, Int. Mater. Rev. 69 (2024) 380–446.
[15] N.H. Abu-Hamdeh, A.A. Melaibari, T.S. Alquthami, A. Khoshaim, H.F. Oztop, A. Karimipour, Efficacy of incorporating PCM into the building envelope on the energy saving and AHU power usage in winter, Sustain Energy Technol Assess 43 (2021) 100969.
[16] J.M. Mahdi, H.I. Mohammed, E.T. Hashim, P. Talebizadehsardari, E.C. Nsofor, Solidification enhancement with multiple PCMs, cascaded metal foam and nanoparticles in the shell-and-tube energy storage system, Appl. Energy 257 (2020) 113993.
[17] C. Lang, C. Wocke, Phase change material thermal storage with constant heat discharge, AIP Conf. Proc. (2018) 2033.
[18] Q. Zhu, P.J. Ong, S.H.A. Goh, R.J. Yeo, S. Wang, Z. Liu, et al., Recent advances in graphene-based phase change composites for thermal energy storage and management, Nano Mater. Sci. 6 (2024) 115–138.
[19] W.B. Fang, C.J. Wang, Heat transfer enhancement analysis of microencapsulated phase change suspension, Appl. Mech. Mater. 361 (2013) 239–243.
[20] M. Benaissa, H.S. Sultan Aljibori, A.M. Abed, J.M. Mahdi, H.I. Mohammed, O. Younis, et al., Maximizing thermal response in latent heat thermal energy storage systems: a comprehensive study of wavy fin configuration and distribution, Int. Commun. Heat Mass Transf. 159 (2024) 108172.
[21] M. Boujelbene, H.I. Mohammed, H.S. Sultan, M. Eisapour, Z. Chen, J.M. Mahdi, et al., A comparative study of twisted and straight fins in enhancing the melting and solidifying rates of PCM in horizontal double-tube heat exchangers, Int. Commun. Heat Mass Transf. 151 (2024) 107224.
[22] N.A.A. Qasem, A. Abderrahmane, A. Belazreg, O. Younis, R.Z. Homod, M. Oreijah, et al., Influence of tree-shaped fins to enhance thermal storage units, Int. Commun. Heat Mass Transf. 151 (2024) 107220.
[23] A.M. Abdulateef, S. Mat, J. Abdulateef, K. Sopian, A.A. Al-Abidi, Geometric and design parameters of fins employed for enhancing thermal energy storage systems: a review, Renew. Sust. Energ. Rev. 82 (2018) 1620–1635.
[24] N.A.A. Qasem, A. Abderrahmane, A. Belazreg, O. Younis, Y. Khetib, K. Guedri, Investigation of phase change heat transfer in a rectangular case as function of fin placement for solar applications, Case Stud. Therm. Eng. 54 (2024) 103996.
[25] A. Belazreg, A. Abderrahmane, N.A.A. Qasem, N. Sene, S. Mohammed, O. Younis, et al., Effect of Y-shaped fins on the performance of shell-and-tube thermal energy storage unit, Case Stud. Therm. Eng. 40 (2022) 102485.
[26] C.C. Wang, On the Airside Performance of Fin-and-Tube Heat Exchangers, 1999.
[27] N. Stathopoulos, M. El Mankibi, R. Issoglio, P. Michel, F. Haghighat, Air–PCM heat exchanger for peak load management: experimental and simulation, Sol. Energy 132 (2016) 453–466.
[28] B.M.S. Punniakodi, R. Senthil, A review on container geometry and orientations of phase change materials for solar thermal systems, J Energy Storage 36 (2021) 102452.
[29] D. Lee, C. Kang, Evaluation of heat storage and release in a double shell and tube heat exchanger with a PCM layer, J. Mech. Sci. Technol. 34 (8) (2020) 3471–3480.
[30] T.M. Ghiwala, D.V.K. Matawla, Sizing of triple concentric pipe heat exchanger, Int. J. Eng. Dev. Res. 2 (2014) 1683–1692.
[31] P.C. Mukesh Kumar, V. Hariprasath, A review on triple tube heat exchangers, Mater Today Proc 21 (2020) 584–587.
[32] D. Akgul, H. Mercan, O. Acikgoz, A.S. Dalkilic, Advances in triple tube heat exchangers regarding heat transfer characteristics of single and two-phase flows in comparison to double tube heat exchangers part 1, Kerntechnik 88 (2023) 642–655.
[33] R. Triki, C. Sirine, B. Mounir, Heat transfer enhancement of phase change materials PCMs using innovative fractal H-shaped fin configurations, J Energy Storage 73 (2023) 109020.
[34] S. Xinguo, I.M. Hayder, T. Mohammadreza Ebrahimnataj, M.M. Jasim, Sh. M. Hasan, W. Zixiong, et al., Investigation of heat transfer enhancement in a triple tube latent heat storage system using circular fins with inline and staggered arrangements, Nanomaterials 11 (2021) 2647.
[35] H. Bilal, I. Muhammad, K. Muhammad Mahabat, U. Saif, Fakhar ul H., Geometric optimization of fin structures for accelerated melting of phase change material in a triplex tube heat exchanger, J Energy Storage 79 (2024) 110162.
[36] D. Fethi, M. Brahim, M. Kouider, K. Sahraoui, S. Lilia, Z. Djallel, Improving the PCM melting process in a triplex tube heat exchanger using a t-shaped fin for thermal energy storage, Stud. Eng. Exact Sci. 5 (2024) e10851.
[37] G.K. Sh, I.M. Hayder, A.H. Karrar, M.M. Jasim, A.A. Waleed Khalid, E. Mohammadreza, et al., Innovative arrangement of circular angled fins for maximizing the discharge performance of triple-tube heat storage systems, Int. J. Low-Carbon Technol. 19 (2024) 938–951.
[38] M.A. Azher, M. Hosseinali Ramezani, B. Jafar, D. Anmar, I.M. Hayder, I. Raed Khalid, et al., Numerical analysis of the energy-storage performance of a PCM-based triplex-tube containment system equipped with arc-shaped fins, Front. Chem. (2022) 10.
[39] M. Boujelbene, J.M. Mahdi, A.M. Abed, M.S. Ghanim, K.A. Hammoodi, H. I. Mohammed, et al., The potential of arch-shaped fins for energy-charge enhancement in triplex-tube heat storage: comparative analysis and optimization, J Energy Storage 79 (2024) 110188.
[40] B. Abdullah, I.M. Hayder, A.-A. Waleed Khalid, D. Anmar, Sh.M. Hasan, T. Pouyan, et al., CFD analysis on optimizing the annular fin parameters toward an improved storage response in a triple tube containment system, Energy Sci. Eng. 10 (2022) 4814–4839.
[41] A.-S. Hashim, K. Masoud Sadeghi, S.A. Aridhee, G. Amir, E. Soroush, S. Mohammad, Performance enhancement of triplex-tube heat storage unit using branched fins during solidification and melting processes: a 2D numerical parametric investigation, Therm. Sci. Eng. Prog. 38 (2023) 101653.
[42] R. Fang, D. Jun, P. Peng Fei, M. Xue-Liang, Analysis of melting and solidification performance of bionic snowflake fin horizontal triplex-tube latent heat storage system based on response surface method, J Energy Storage 70 (2023) 108067.
[43] Y. Yan, Z. Xiaowei, D. Hongbing, W. Chuang, Performance of Triangular Finned Triple Tubes with Phase Change Materials (PCMs) for Thermal Energy Storage, 2021, pp. 869–874.
[44] A. Standard, Thermal Environmental Conditions for Human Occupancy 55, ANSI/ASHRAE, 1992, p. 5.
[45] GmbH R, Product Information, Data Sheet of RT25, 2025.
[46] A. Brent, V. Voller, K. Reid, Enthalpy-porosity technique for modeling convection-diffusion phase change: application to the melting of a pure metal, Numer. Heat Transf. A Appl. 13 (1988) 297–318.
[47] A.S. Soliman, A.A. Sultan, M.A. Sultan, Effect of mushy zone parameter on phase change behavior of different configurations storage unit: numerical simulation and experimental validation, Sustainability 14 (2022) 14540.
[48] M. Longeon, A. Soupart, J.-F. Fourmigué, A. Bruch, P. Marty, Experimental and numerical study of annular PCM storage in the presence of natural convection, Appl. Energy 112 (2013) 175–184.
[49] A.A. Al-Abidi, S. Mat, K. Sopian, M.Y. Sulaiman, A.T. Mohammad, Experimental study of melting and solidification of PCM in a triplex tube heat exchanger with fins, Energ. Build. 68 (2014) 33–41.